

Flapping dynamics of a flag in a uniform stream

BENJAMIN S. H. CONNELL[†] AND DICK K. P. YUE[‡]

Department of Mechanical Engineering, Massachusetts Institute of Technology,
Cambridge, MA 02139, USA

(Received 6 March 2006 and in revised form 15 November 2006)

We consider the flapping stability and response of a thin two-dimensional flag of high extensional rigidity and low bending rigidity. The three relevant non-dimensional parameters governing the problem are the structure-to-fluid mass ratio, $\mu = \rho_s h / (\rho_f L)$; the Reynolds number, $Re = VL/\nu$; and the non-dimensional bending rigidity, $K_B = EI / (\rho_f V^2 L^3)$. The soft cloth of a flag is represented by very low bending rigidity and the subsequent dominance of flow-induced tension as the main structural restoring force. We first perform linear analysis to help understand the relevant mechanisms of the problem and guide the computational investigation. To study the nonlinear stability and response, we develop a fluid–structure direct simulation (FSDS) capability, coupling a direct numerical simulation of the Navier–Stokes equations to a solver for thin-membrane dynamics of arbitrarily large motion. With the flow grid fitted to the structural boundary, external forcing to the structure is calculated from the boundary fluid dynamics. Using a systematic series of FSDS runs, we pursue a detailed analysis of the response as a function of mass ratio for the case of very low bending rigidity ($K_B = 10^{-4}$) and relatively high Reynolds number ($Re = 10^3$). We discover three distinct regimes of response as a function of mass ratio μ : (I) a small μ regime of fixed-point stability; (II) an intermediate μ regime of period-one limit-cycle flapping with amplitude increasing with increasing μ ; and (III) a large μ regime of chaotic flapping. Parametric stability dependencies predicted by the linear analysis are confirmed by the nonlinear FSDS, and hysteresis in stability is explained with a nonlinear softening spring model. The chaotic flapping response shows up as a breaking of the limit cycle by inclusion of the 3/2 superharmonic. This occurs as the increased flapping amplitude yields a flapping Strouhal number ($St = 2Af/V$) in the neighbourhood of the natural vortex wake Strouhal number, $St \simeq 0.2$. The limit-cycle von Kármán vortex wake transitions in chaos to a wake with clusters of higher intensity vortices. For the largest mass ratios, strong vortex pairs are distributed away from the wake centreline during intermittent violent snapping events, characterized by rapid changes in tension and dynamic buckling.

1. Introduction

The flag flapping problem is of interest not only for its prevalence, but also for the simplicity of the problem statement and the richness of the behaviour. While we observe this phenomenon often in our daily lives, recent work suggests possible application of natural flapping behaviour to the pursuit of turbulence reduction (Shen *et al.* 2003; Techet, Hover & Triantafyllou 1997) and energy generation (Allen & Smits

[†] Present address: Applied Physical Sciences Corporation, Groton, CT 06340, USA.

[‡] Author to whom correspondence should be addressed: yue@mit.edu

2001), as well as aiding in efficient propulsive swimming (Liao *et al.* 2003*a, b*). The general problem is one of a thin membrane in an unbounded fluid flow which is held pinned at the leading edge and is free at the trailing edge. As the flow travels over the body surface, off the trailing edge, and into the wake, an instability can be realized which manifests itself as sustained flapping of the body. The system includes the dynamic effects of the flow over the undulating membrane, vorticity generation at the surface, vortex shedding at the trailing edge, structural inertia, restoring due to bending rigidity, and restoring due to the flow-induced variable tension in the body. In this study, we restrict ourselves to the two-dimensional problem. The three-dimensional case is more involved but exhibits the salient behaviours and features of the two-dimensional problem we discuss here (Connell 2006). Our interest is in the case of very low bending rigidity typical of cloth, where the flag's structural restoring force is dominated by flow-induced tension. If we further restrict ourselves to the case of high extensional rigidity, the system is governed by three relevant non-dimensional parameters associated with the structure-to-fluid mass ratio, the bending rigidity, and the Reynolds number, given, respectively, by

$$\mu = \frac{\rho_s h}{\rho_f L}, \quad K_B = \frac{EI}{\rho_f V^2 L^3}, \quad \text{and} \quad Re = \frac{VL}{\nu}, \quad (1.1)$$

for a two-dimensional body of length L , mass-per-length $\rho_s h$, and bending rigidity EI , in a fluid flow of density ρ_f , viscosity ν , and flow speed V . In realistic flag-like problems, the bending rigidity is very low and the dynamics are primarily governed by the mass ratio and the Reynolds number.

The present work builds upon earlier studies of passive flapping dynamics, enhancing the understanding of the coupled physics through a range of flag flapping response modes. An early study of Paidoussis (1966) treats the problem of the stability and response of a flexible cylinder in axial flow, both theoretically and experimentally. He notes the destabilizing effect of increasing the flow velocity through what is essentially the Kelvin–Helmholtz instability, balanced against the restoring effect of tension and bending rigidity of the flexible body. Predictions and observation of a streamwise travelling-wave flapping solution are found, similar to the motion of swimming fish observed by Gray (1933). Paidoussis emphasizes the importance of the nonlinear effects neglected in the theoretical model when considering the unstable response of the experiments. Subsequent work of Triantafyllou (1992) examines the nature of the travelling-wave linear instability in further detail. Coene (1992) extends the Paidoussis theoretical analysis to that of a thin membrane. For this case, the contribution of the flow is different in that the added mass can no longer be considered sectionally with strip theory, but becomes a function of the mode of oscillation. The case of constant tension of the membrane is considered, and experiments are performed with paper strips pulled at both ends. Critical values of the tension, below which flapping is realized, are found experimentally to be in good agreement with theory. Two important considerations for the flag flapping problem not incorporated in these studies are the interaction of the flow wake and the varying tension along the length associated with the fluid-dynamic forcing.

Including the existence and influence of the flow wake adds considerable complexity to the theoretical treatment. Such an analysis including the shedding of wake vortices is presented in Argentina & Mahadevan (2005). Their approach details a method for including finite-length effects, and an analysis is given for a particular case which simplifies the formulation. Trends are predicted for the flapping frequency and critical flow speed above which flapping is realized. In this case the added mass is much smaller

than the structural mass, the flow speed is much larger than the flapping velocity, and the bending rigidity dominates the structural restoring force – conditions which do not obtain for the regime of interest in the present study. The analysis of Moretti (2003) considers in detail the sources and influence of tension in the body, citing the original work of Thoma (1939), which highlights the importance of dynamically induced tension. These papers explain that, during active flapping, the tension induced by the flapping motion becomes very significant, and Moretti (2004) hypothesizes that it is this dynamically induced tension which limits the flapping amplitude.

The difficulties and assumptions of theoretical treatment are avoided through the use of experiments and numerical simulations. The experiment of Zhang *et al.* (2000), using a filament in a flowing soap film, allowed for the effects of wake flow and varying structural tension. Using a film to maintain two-dimensionality, the experiment observed both stable and unstable responses, depending on the filament length. As the length was increased, the filament became unstable, displaying a streamwise travelling-wave response. The flapping amplitude was observed to diminish toward the leading edge, where the tension due to viscous forcing and gravity was highest. A region of bistability was observed, where sufficiently large perturbation could transform the system from a stable to an unstable response.

Two distinct approaches to numerically simulating the Zhang soap film experiments have been made by Zhu & Peskin (2002; 2003) and Farnell, David & Barton (2004*a, b*). The Farnell *et al.* work treats the filament as a pendulum of many links connected by springs and dashpots. Such treatment requires tuning of the model, and it is indicated that further work is required in determining the accuracy of the approach. The Zhu & Peskin numerical study uses the immersed boundary method to couple a nonlinear filament with bending and extensional rigidity to a Navier–Stokes solver. The study replicates the trends found in the experiment. These include the transition to unstable flapping for longer filaments and the existence of a bistable region. Flow visualization indicates that the small-scale vortical structures observed in the experiment were not apparent in the simulations, an anticipated result with the Reynolds number having been reduced from 20 000 in the experiment to 200 in the simulation. It is noted that removing the filament mass results in an always stable filament. Beyond this observation, the variation parameter used for the soap film studies is the dimensional filament length, which influences the three non-dimensional parameters, μ , Re , and K_B .

The experimental investigation of paper flutter in a wind tunnel of Watanabe *et al.* (2002) illustrates the importance of this flapping problem to paper moving through a printing press. Through a series of experiments, the stabilizing effects of decreasing flow velocity, decreasing length, decreasing mass, and increasing bending rigidity were presented. Again, a bistable region was discovered in the transition from stable to unstable flapping modes. Increasing the flow speed from the critical point, the flapping amplitude and the Strouhal number were found to increase, both approaching asymptotic values in the established flapping regime. While the Watanabe *et al.* experiments were performed in air, the recent work of Shelley, Vandenberghe & Zhang (2005) details similar experiments performed in a water tunnel. These experiments in water required special treatment to bring the membrane mass up to a sufficient value to realize flapping. Similar results to those of the air experiments were found for stability, response, and bistability with changing flow velocity, which translates to variations in the non-dimensional parameters Re and K_B .

In the present work, we consider the two-dimensional flag problem in an unbounded fluid domain. The effects of Reynolds number, structure-to-fluid mass ratio, and non-dimensional bending rigidity on the system stability are examined. For the case of

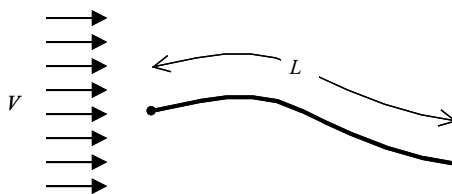


FIGURE 1. Depiction of the problem of the flapping two-dimensional flag of length L in uniform incoming flow V in an unbounded fluid domain. The flag is pinned at the leading edge and free at the trailing edge.

very low bending rigidity, we study the progression of response in relation to the system mass ratio to understand the physics related to the range of observed flag flapping behaviour.

We first perform a linear analysis to show how the relevant non-dimensional parameters of the system influence the realization of the flapping instability. The structural tension in this theoretical stability analysis is modelled as a function of the Reynolds number through boundary layer theory, and no attempt is made to model the wake effects in the linear analysis as did Argentina & Mahadevan (2005). To examine the full nonlinear flapping problem, including wake effects and variable tension in the body, we develop a coupled fluid-structure direct simulation (FSDS) of the Navier–Stokes equations and geometrically nonlinear structural equations. We perform a systematic series of FSDS runs to understand the trends of stability and response for the flag flapping problem. The simulations corroborate the stability criteria identified in the linear analysis: a destabilizing effect of increasing structure-to-fluid mass ratio, where a lesser proportion of the inertia is convecting with the flow as added mass; and a stabilizing effect of higher bending rigidity and lower Reynolds number, both of which increase the structural restoring force. For the case of very low bending rigidity and low-to-moderate Reynolds numbers ($Re = 100 \rightarrow 5000$) considered, increasing the mass ratio is found to transition the system through three distinct response regimes: (I) fixed-point stability, (II) limit-cycle flapping, and (III) chaotic flapping; each with representative wake characteristics.

Section 2 defines the problem and the relevant parameters, while the approach for nonlinear simulation is described in §3. Linear analysis for the fixed-point stability problem is developed in §4.1, with simulation results for stability and flapping response discussed in §4.2. A summary of the findings is provided in §5.

2. Problem statement

We consider the problem of a two-dimensional thin membrane, pinned on the leading edge and free on the trailing edge, excited by a uniform incompressible viscous inflow in an unbounded domain, shown in figure 1. The body is sufficiently thin so that the small thickness (and its variation with length) is unimportant to the result. The structural properties of the membrane in this two-dimensional study are the length, mass-per-length, bending rigidity, and extensional rigidity. The extensional rigidity is considered to be very high, and is included in the nonlinear numerical model as a means of maintaining continuity and transmitting force tangentially, as detailed in §3.2.

The geometrically nonlinear equation of motion for the two-dimensional flag is

$$\rho_s h \frac{\partial^2 \mathbf{x}}{\partial t^2} - \frac{\partial}{\partial s} \left(T(s) \frac{\partial \mathbf{x}}{\partial s} \right) + EI \frac{\partial^4 \mathbf{x}}{\partial s^4} = \mathbf{F}_f, \quad (2.1)$$

with s as the Lagrangian coordinate along the length, and the body position vector \mathbf{x} fixed at the pinned leading edge. Here, ρ_s is the structural density, h is the flag thickness, $T(s)$ is the tension in the body, and EI is the structural bending rigidity. Fluid coupling comes through the forcing term defined as

$$\mathbf{F}_f = [\Delta \tau] \hat{n}, \quad (2.2)$$

where \hat{n} is the upward facing normal and $[\Delta \tau]$ is the difference between the fluid-dynamic stress tensor at the top and bottom of the body. Elements of the stress tensor are defined by the fluid dynamics at the body surface as

$$\tau_{ij} = \nu \rho_f \left(\frac{\partial u_i}{\partial \xi_j} + \frac{\partial u_j}{\partial \xi_i} \right) - \delta_{ij} p. \quad (2.3)$$

Equations (2.2) and (2.3) contain all of the physical influence of the fluid flow on the flexible structure. This includes viscous damping and boundary layer drag, inertial added mass effect, and the influence of separation and vortices shedding into the wake.

The fluid dynamics are obtained as the solution to the incompressible fluid momentum and mass conservation equations, the Navier–Stokes equations, written as

$$\frac{\partial \mathbf{v}}{\partial t} + (\mathbf{v} \cdot \nabla) \mathbf{v} = -\frac{1}{\rho_f} \nabla p + \nu \nabla^2 \mathbf{v}, \quad (2.4)$$

$$\nabla \cdot \mathbf{v} = 0. \quad (2.5)$$

The velocity boundary conditions complete the problem specification:

$$\mathbf{v} = \frac{\partial \mathbf{x}}{\partial t} \quad \text{on flag boundary}, \quad (2.6)$$

$$\mathbf{v} = \mathbf{V} \quad \text{at } \infty. \quad (2.7)$$

It is through this inner boundary condition (2.6) that the structural influence is imparted to the fluid, so that the flow solution is consistent with the structural motion. While dynamic continuity between the fluid and structural domains is contained in (2.1)–(2.3), kinematic continuity between the domains is contained in (2.4)–(2.7). This set of equations governs the coupled fluid and structural motion of the system depicted in figure 1.

3. The coupled numerical model: FSDS

We develop a coupled fluid–structure direct simulation (FSDS) method to study the coupled nonlinear problem. The fluid-dynamic direct simulation (FDS) is a finite-difference solution to the Navier–Stokes equations solved on a grid fitted to a moving thin body. Fluid-dynamic forcing on the body surface is calculated and used as input to a finite-difference structural-dynamic direct simulation (SDS). The structural solver is geometrically nonlinear and able to take on arbitrary configurations. Both the FDS and SDS are implicit, requiring iteration between the two for convergence at each time step.

3.1. The fluid-dynamic numerical model: FDS

Direct solution of the Navier–Stokes equation is carried out using primitive variables (p , \mathbf{v}) on a moving collocated grid. An O-grid is used for discretization, and is shown

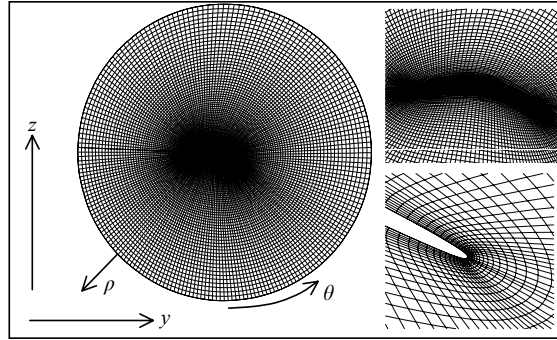


FIGURE 2. Grid used for FDS with computational (ρ, θ) and physical (y, z) directions indicated. Zoomed view of grid clustering at the body and wrapping around the end.

with the computational (ρ, θ) and physical (y, z) coordinate directions indicated in figure 2. The body thickness is tapered and rounded at the ends. The grid is generated using the elliptic solution method of Thompson, Thames & Mastin (1977), with the clustering source terms calculated from an algebraically generated grid around a straight foil. With coordinate dependencies of $y(\rho, \theta, \tau)$, $z(\rho, \theta, \tau)$, and $t(\tau)$, the derivatives can be mapped from physical to computational space, utilizing the Jacobian for spatial derivatives and grid velocities for calculation of the time derivative on a moving grid.

The mapped derivatives are used in the Navier–Stokes equation, hereafter made non-dimensional by the body length L , incoming flow V , and fluid density ρ_f :

$$\frac{\partial \mathbf{v}}{\partial t} + (\mathbf{v} \cdot \nabla) \mathbf{v} = -\nabla p + \frac{1}{Re} \nabla^2 \mathbf{v}. \quad (3.1)$$

The time integration method used is the second-order backwards difference scheme (BDF2), as discussed in Li & Tang (2001) and Strikwerda (1997). This implicit method offers stability with second-order accuracy, and gives (3.1) the semi-discrete form

$$\frac{3\mathbf{v}^{n+1} - 4\mathbf{v}^n + \mathbf{v}^{n-1}}{2\Delta t} + ((\mathbf{v}^{n+1} - \mathbf{v}_g^{n+1}) \cdot \nabla) \mathbf{v}^{n+1} = -\nabla p^{n+1} + \frac{1}{Re} \nabla^2 \mathbf{v}^{n+1}, \quad (3.2)$$

where \mathbf{v}_g is the velocity of the moving computational grid. All spatial derivatives are taken as second-order centred differences, excepting those in the convective term which use the third-order upwinding scheme of Kawamura & Kuwahara (1984) (see also Li 1997).

The pressure is found with a Poisson equation obtained with the projection method of Chorin (1968) (see also Armfield 1991). The equation is formed by taking the discrete divergence of (3.2) and setting the discrete velocity divergence equal to zero. Pressure boundary conditions are derived for consistent zero velocity divergence. This boundary treatment, with the implementation of a solvability condition, couples the otherwise chessboard-independent grids inherent to the Chorin scheme.

Verification and validation of FDS

For the fluid-dynamics simulation (FDS) portion of the coupled code, we perform full convergence testing uses the benchmarking problem of a harmonically driven cylinder, studied experimentally and numerically by Dutsch *et al.* (1998). We calculate the drag coefficient c_d and added mass coefficient c_i for the case of $Re = 100$ and

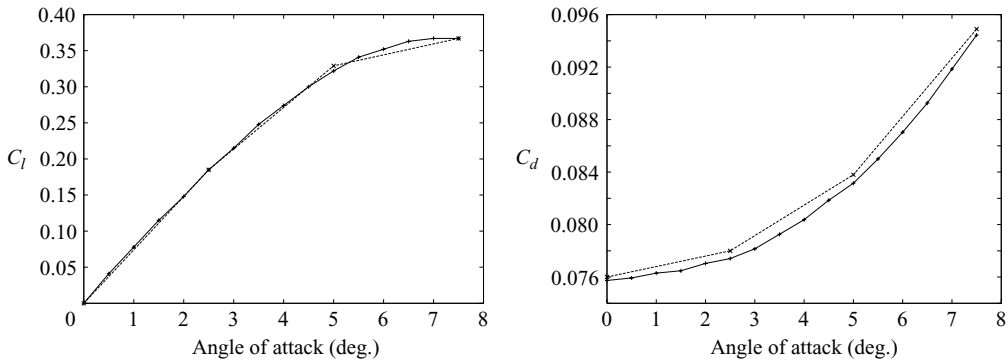


FIGURE 3. Lift (c_l) and drag (c_d) coefficients vs. angle of attack for a NACA0008 at $Re = 2000$, for simulations of Kunz & Kroo (2001) (—+—) and the present FDS (× —).

$KC = 5$. Using $N \times N$ grids of dimension $N = (40, 60, 80, 100, 140, 200)$, second-order convergence of the forcing error is found as $e_{cd} \sim \Delta x^{1.65}$ and $e_{ci} \sim \Delta x^{1.92}$. Varying the time step as $\Delta t = (0.1, 0.05, 0.025, 0.01, 0.005, 0.0025)$, second-order convergence of the error is found as $e_{cd} \sim \Delta t^{2.21}$ and $e_{cm} \sim \Delta t^{1.84}$. Convergence is also found with increasing domain size, as the influence of the far-field boundaries is reduced. The converged values of $c_d = 2.09$ and $c_i = 1.45$ are the same values reported by Dutsch *et al.* for their highest-resolution result. Success with this problem indicates dynamic accuracy of the flow solver in a simulation involving a moving grid.

We further validate the FDS using a more difficult geometry of a foil. The solution of a fixed NACA0008 foil at a range of angles of attack and $Re = 2000$ is compared to the simulations of Kunz & Kroo (2001) in figure 3. The plots of lift coefficient c_l and drag coefficient c_d with angle of attack show the results to be consistent to within 2.2%, and capturing the onset of stall. Similar validation was performed for an impulsively started thin foil (0.02 thickness ratio), and compare well to the experiments of Dickinson & Gotz (1993), as detailed in Connell (2006).

3.2. The structural-dynamic numerical model: SDS

A structural solver is developed which allows for arbitrary orientation and configuration of the thin body, and which offers stability through a range of external forcing scenarios. We are primarily interested in simulating an inextensible body with no bending rigidity. Physically, this would correspond to a material of infinite modulus of elasticity (to achieve inextensibility) and infinitesimal thickness (to eliminate bending stiffness). For a robust capability, able to accommodate loss of positive tension (see Triantafyllou & Howell 1994), we consider finite physical parameters of very large modulus and very small thickness, corresponding to a body which is slightly extensible with very weak bending rigidity.

The equations of motion are derived in Cartesian coordinates using Hamilton's principle, linearizing around small body thickness and extensional strain. The final equations are equivalent to those used for the structural component in Zhu & Peskin (2002), and permit arbitrary configuration and orientation of the body:

$$\rho h \frac{\partial^2 \mathbf{x}}{\partial t^2} - Eh \frac{\partial}{\partial s} \left[\left(1 - \left(\frac{\partial \mathbf{x}}{\partial s} \cdot \frac{\partial \mathbf{x}}{\partial s} \right)^{-1/2} \right) \frac{\partial \mathbf{x}}{\partial s} \right] + \frac{Eh^3}{12} \frac{\partial^4 \mathbf{x}}{\partial s^4} = \mathbf{F}, \quad (3.3)$$

with natural free-end boundary conditions of

$$-Eh \left(1 - \left(\frac{\partial \mathbf{x}}{\partial s} \cdot \frac{\partial \mathbf{x}}{\partial s} \right)^{-1/2} \right) \frac{\partial \mathbf{x}}{\partial s} + \frac{Eh^3}{12} \frac{\partial^3 \mathbf{x}}{\partial s^3} = 0, \quad \text{and} \quad \frac{\partial^2 \mathbf{x}}{\partial s^2} = 0, \quad (3.4)$$

where s is the Lagrangian coordinate along the length. Non-dimensionalizing by L , V , and ρ_f , as with (3.1), we obtain the equation of motion

$$\mu \frac{\partial^2 \mathbf{x}}{\partial t^2} - K_S \frac{\partial}{\partial s} \left[\left(1 - \left(\frac{\partial \mathbf{x}}{\partial s} \cdot \frac{\partial \mathbf{x}}{\partial s} \right)^{-1/2} \right) \frac{\partial \mathbf{x}}{\partial s} \right] + K_B \frac{\partial^4 \mathbf{x}}{\partial s^4} = \mathbf{F}, \quad (3.5)$$

where

$$\mu = \frac{\rho_s h}{\rho_f L}, \quad K_S = \frac{Eh}{\rho_f V^2 L}, \quad \text{and} \quad K_B = \frac{EI}{\rho_f V^2 L^3}. \quad (3.6)$$

This structural equation is also solved with an implicit second-order finite-difference formulation in space and time, so that the semi-discrete equation of motion is

$$\mu \frac{2\mathbf{x}^{n+1} - 5\mathbf{x}^n + 4\mathbf{x}^{n-1} - \mathbf{x}^{n-2}}{\Delta t^2} - K_S \frac{\partial}{\partial s} \left[\left(1 - \left(\frac{\partial \mathbf{x}^{n+1}}{\partial s} \cdot \frac{\partial \mathbf{x}^{n+1}}{\partial s} \right)^{-1/2} \right) \frac{\partial \mathbf{x}^{n+1}}{\partial s} \right] + K_B \frac{\partial^4 \mathbf{x}^{n+1}}{\partial s^4} = \mathbf{F}^{n+1}. \quad (3.7)$$

We employ an iterative solver for solution of the nonlinear equation (3.7). When the forcing term comes from the coupled fluid dynamics it is also a function of \mathbf{x} at the $(n+1)$ th time step, one that requires solution of the flow through the entire domain. The requirement for simultaneous solution of the structure and fluid is satisfied by iterating between the two solvers at any given time step. With sufficient convergence of both the structural and fluid dynamics, the coupled system is then advanced in time.

Verification and validation of SDS

For verification and validation of the structural solver, we consider problems of a body pinned at one end and hanging or swinging under the influence of gravity. Comparison was made to the Bessel equation solution to the linear problem, and frequency errors of under 2% were found for the two lowest modes where nonlinear effects are minimal (see Connell 2006). The nonlinear problem of a horizontally pinned cable released at one end was studied experimentally and numerically by Koh, Zhang & Quek (1999). The time history of the pinned-end tension is shown with that obtained from the present study in figure 4. The numerical results from the present and earlier work follow each other closely, and both differ slightly from those obtained experimentally.

The problem of harmonically forcing a hanging chain horizontally at its attached end was used to compare simulations to experiment by Howell & Triantafyllou (1993) and Gobat, Grosenbaugh & Triantafyllou (2002). Simulation accuracy was gauged by its success in capturing an initial loop-closing event observed experimentally at time $t \simeq 3.4$ s. Figure 5 shows the present simulation result with the body closing on itself at $t = 3.48$ s. This timing of the event, and the size and location of the loop, compare very well to the detailed study of Gobat *et al.* (2002). The plot showing the entire length of chain displays the very small scale of the loop, and a rigidity ratio of $K_S/K_B = 4 \times 10^7$ was required to obtain this resolution. Such tight loop closing is far beyond the expected requirements of the coupled fluid-structure solver.

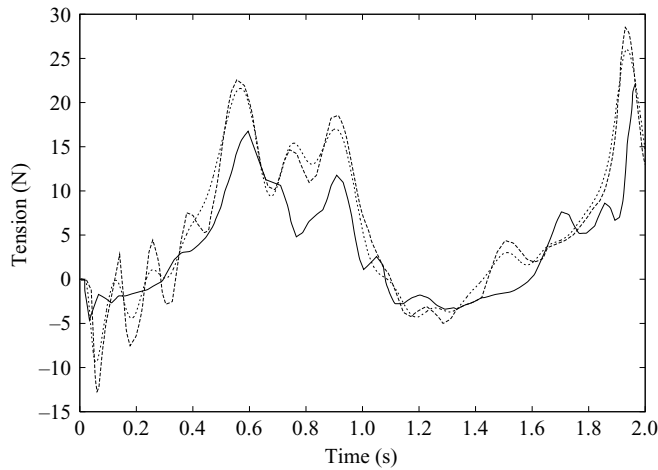


FIGURE 4. Time history of the attached-end tension of a horizontally pinned cable under the influence of gravity released at one end, for the Koh *et al.* (1999) experiment (—) and simulation (---), and the present SDS (····).

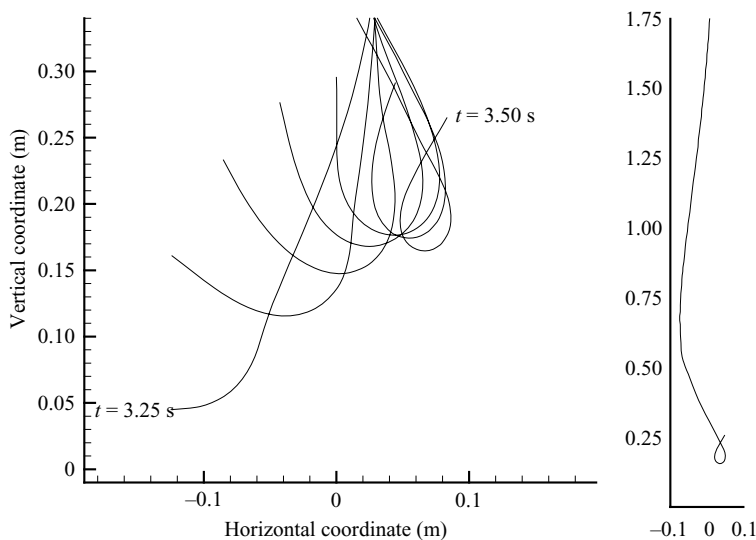


FIGURE 5. Loop-closing event at the free end of a chain hanging under the influence of gravity and harmonically forced horizontally at the attached end, from SDS simulation of the shaking chain experiment. The snapshot at right shows the entire length of the chain.

3.3. Coupling the FDS and SDS

The solution of the fluid and structural solvers, with both using implicit formulations, must be simultaneous. The coupled FSDS solver requires iteration between the velocity field, pressure field, and structural position, where updating the structural position requires recalculation of the flow grid. A stability problem is encountered with this iteratively coupled method when the body mass μ is reduced. As the added mass becomes the dominant inertial effect, a larger portion of the inertia is represented on the right-hand side of the structural equation (3.5). The problem is stabilized by assuming an added mass value \tilde{m}_a , and subtracting the added mass component from

the fluid forcing, with the acceleration term on the right-hand side being that from the previous $(m - 1)$ th iteration. That is,

$$(\mu + \tilde{m}_a) \frac{\partial^2 \mathbf{x}}{\partial t^2} - K_s \frac{\partial}{\partial s} \left[\left(1 - \left(\frac{\partial \mathbf{x}}{\partial s} \cdot \frac{\partial \mathbf{x}}{\partial s} \right)^{-1/2} \right) \frac{\partial \mathbf{x}}{\partial s} \right] + K_B \frac{\partial^4 \mathbf{x}}{\partial s^4} = \mathbf{F}_f + \tilde{m}_a \left(\frac{\partial^2 \mathbf{x}}{\partial t^2} \right)^{m-1}. \quad (3.8)$$

Upon convergence of the system, the \tilde{m}_a terms on each side of (3.8) cancel, and the precise choice of the assumed added mass value does not impact the solution. This procedure is effective in stabilizing the coupled solution, even with vanishing body mass.

Verification of the coupled FSDS

We perform FSDS on a pinned thin foil with impulsively started cross-flow at $Re = 1000$ using two different resolution grids of $N = (60 \times 120)$ and $N = (100 \times 200)$. With the relatively high values for the mass ratio ($\mu = 1$) and bending rigidity ($K_B = 0.1$), there is significant energy exchange between the fluid and structure. The progression of the coupled solution in time is depicted in the series of vorticity plots of figure 6(a), which show the vortices shedding and interacting with the nonlinear body motion as it aligns with the flow. A particularly good measure of accuracy of the coupled simulation is energy conservation, and we plot the energy budget for the lower- and higher-resolution FSDS in figure 6(b). Significant energy content appears in all components except the structural extensional mode, indicating the near-inextensibility. The structural energies and the outer boundary flux (representing energy input to the system through a pressure gradient) are not significantly influenced by the grid resolution, while the fluid kinetic energy and fluid dissipation both show lower values on the lower-resolution grid. This additional energy loss, or numerical dissipation, is displayed in the curves of total loss. At the end of the simulation, the low-resolution numerical dissipation is 53 % of the physical viscous dissipation, while the high-resolution numerical dissipation is 24 % of the viscous dissipation, indicating improved Reynolds number accuracy. This higher-resolution $N = (100 \times 200)$ grid is used for all the simulations for the present study.

4. Results and discussion

Before studying the nonlinear coupled problem using a systematic series of FSDS simulations, we first perform a linear analysis of the flapping foil to obtain the linear stability as a function of the relevant non-dimensional parameters. This analysis delineates the fundamental physical modes of the problem and offers guidance to the FSDS numerical study. The FSDS results complete the bigger picture of the full nonlinear problem, including trends in the system stability and regimes of unstable response.

We proceed in the framework of the relevant non-dimensional parameters of the system, given by (1.1). While dimensional physical parameters such as body length or flow speed influence more than one physical effect, use of non-dimensional parameters isolates the physical influences to the system, facilitating analysis and interpretation.

4.1. Linear stability analysis

Following the work of Triantafyllou (1992) and Coene (1992), we write the equation of motion for the foil, considering z to be the displacement from the streamwise y

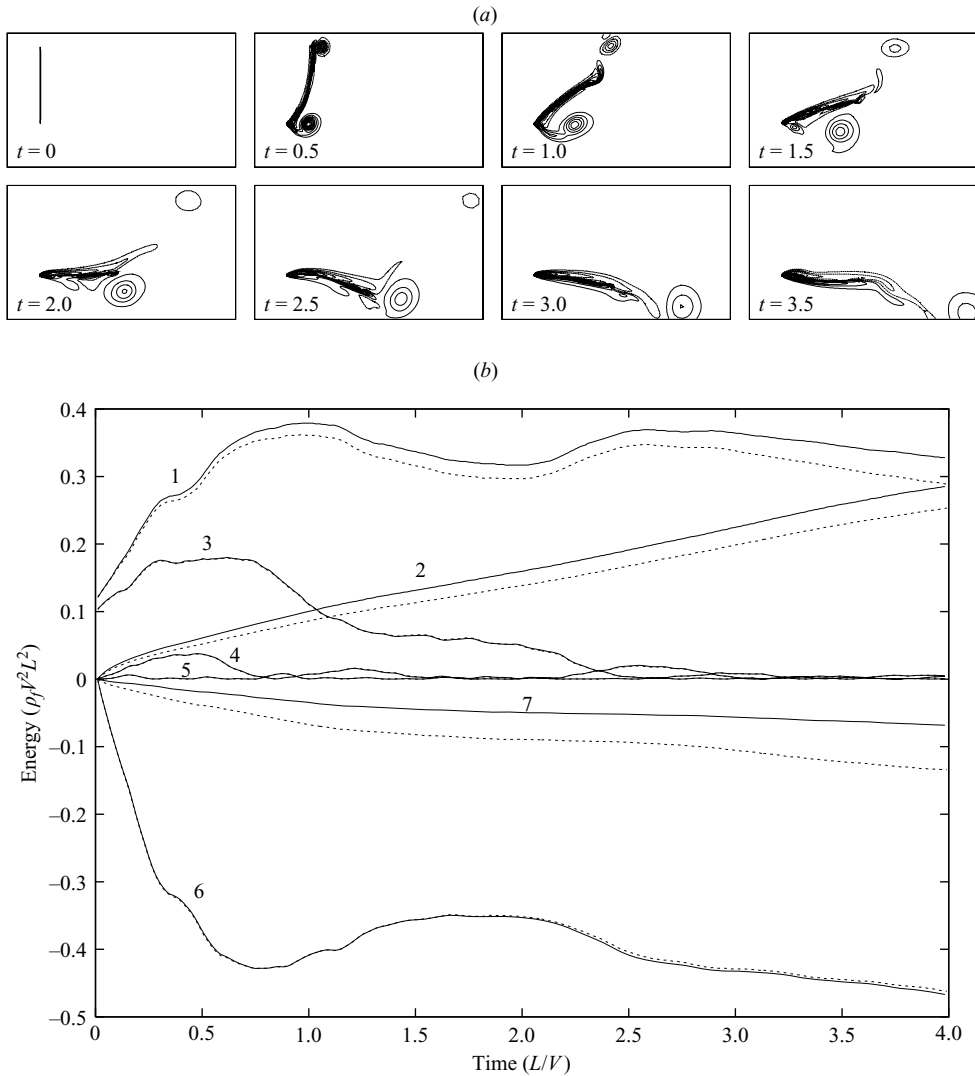


FIGURE 6. FSDS simulation of a flexible body pinned at the leading edge subject to an impulsively started cross-flow. (a) Vorticity contour series. (b) Energy budget time history using grids of $N = (60 \times 120)$ (---) and $N = (100 \times 200)$ (—), for fluid-kinetic (1), fluid-dissipated (2), structural-kinetic (3), structural-bending potential (4), structural-extensional potential (5), outer boundary flux (6), and total loss (7) energies.

axis, as

$$\rho_s h \frac{\partial^2 z}{\partial t^2} - \frac{\partial}{\partial y} \left(T \frac{\partial z}{\partial y} \right) + EI \frac{\partial^4 z}{\partial y^4} + m_a \left(\frac{\partial}{\partial t} + V \frac{\partial}{\partial y} \right)^2 z = 0. \quad (4.1)$$

The only difference between (4.1) and those of Triantafyllou and Coene is that we have allowed for variation of the tension in the streamwise direction. Unlike the soap film problem where gravity influences the tension, the present study has only the fluid forcing contributing to the tension. If we assume the fluid forcing to be that due to a

Blasius laminar boundary layer, the tension can be written as

$$T(y) = 1.3\rho_f V^2 L Re^{-1/2} \left(1 - \sqrt{\frac{y}{L}}\right), \quad (4.2)$$

where

$$Re = \frac{VL}{\nu}. \quad (4.3)$$

In seeking a solution to (4.1) which lends itself to physical interpretation, we avoid the variable tension expression of (4.2), instead using the maximum value of (4.2) evaluated at $y=0$ as a constant value along the length. Using a constant value for tension, we revert to the equation used in the previous studies, the notable difference being the quantifying of the tension in terms of the fluid dynamics. The equation of motion is now written with the last term expanded as

$$\rho_s h \frac{\partial^2 z}{\partial t^2} - 1.3\rho_f V^2 L Re^{-1/2} \frac{\partial^2 z}{\partial y^2} + EI \frac{\partial^4 z}{\partial y^4} + m_a \frac{\partial^2 z}{\partial t^2} + 2m_a V \frac{\partial^2 z}{\partial y \partial t} + m_a V^2 \frac{\partial^2 z}{\partial y^2} = 0. \quad (4.4)$$

The three expanded final terms represent the fluid-dynamic effects of inertial added mass, Coriolis force, and centrifugal force, respectively (see Triantafyllou 1992). Grouping the terms, we have

$$(\rho_s h + m_a) \frac{\partial^2 z}{\partial t^2} + (m_a V^2 - 1.3\rho_f V^2 L Re^{-1/2}) \frac{\partial^2 z}{\partial y^2} + EI \frac{\partial^4 z}{\partial y^4} + 2m_a V \frac{\partial^2 z}{\partial y \partial t} = 0. \quad (4.5)$$

In the second term, the countering effects of the Kelvin–Helmholtz instability and the restoring action of the drag-induced tension can be seen. The variables (y, z, t) of the equation of motion are now non-dimensionalized by the length L and free-stream velocity V , obtaining

$$(\rho_s h + m_a) \frac{V^2}{L} \frac{\partial^2 z}{\partial t^2} + (m_a V^2 - 1.3\rho_f V^2 L Re^{-1/2}) \frac{1}{L} \frac{\partial^2 z}{\partial y^2} + EI \frac{1}{L^3} \frac{\partial^4 z}{\partial y^4} + 2m_a V \frac{V}{L} \frac{\partial^2 z}{\partial y \partial t} = 0. \quad (4.6)$$

Dividing through by $V^2 \rho_f$, we obtain the final form of the non-dimensional equation:

$$(\mu + c_m) \frac{\partial^2 z}{\partial t^2} + (c_m - 1.3Re^{-1/2}) \frac{\partial^2 z}{\partial y^2} + K_B \frac{\partial^4 z}{\partial y^4} + 2c_m \frac{\partial^2 z}{\partial y \partial t} = 0, \quad (4.7)$$

where $c_m = m_a/(\rho_f L)$.

We assume a travelling-wave mode, $z = A e^{i(ky - \omega t)}$, where k and ω are the non-dimensional wavenumber and frequency. The equation of motion then yields the dispersion relation:

$$(\mu + c_m)\omega^2 + (c_m - 1.3Re^{-1/2})k^2 - K_B k^4 - 2c_m \omega k = 0. \quad (4.8)$$

Solving for the frequency, we have

$$\begin{aligned} \omega &= \frac{c_m k}{\mu + c_m} \pm \frac{1}{\mu + c_m} \sqrt{c_m^2 k^2 - (\mu + c_m)(c_m k^2 - 1.3Re^{-1/2} k^2 - K_B k^4)} \\ &= \frac{c_m k}{\mu + c_m} \pm \frac{k}{\mu + c_m} \sqrt{-\mu c_m + (\mu + c_m)(1.3Re^{-1/2} + K_B k^2)}. \end{aligned} \quad (4.9)$$

Unstable flapping modes are realized when the argument of the radical in (4.9) is negative, i.e.

$$\frac{\mu c_m}{\mu + c_m} > 1.3Re^{-1/2} + K_B k^2. \quad (4.10)$$

As expected, we see from (4.9) that the tension and bending rigidity are stabilizing effects, while the centrifugal force is the destabilizing effect of the Kelvin–Helmholtz instability. All three of these effects are scaled by the total inertia, the sum of structural mass and added mass. An additional stabilizing effect comes from the Coriolis force (the first term in the radical), which scales only with the added mass. As the expression in the radical can never become negative when $\mu = 0$, the system cannot realize unstable flapping without structural mass. Zhu & Peskin (2002) indicate that the periodic energy exchange between potential energy and kinetic energy cannot be sustained unless the structure itself can take on kinetic energy, and that having the kinetic energy in terms of added mass alone is not sufficient. The present analysis shows why that is the case. The fluid added mass is advected with the flow velocity, and, thus, influences the system differently from the structural mass. It is, in fact, the added mass which brings about the flapping instability, but this instability cannot be realized on a massless body.

From potential flow solution, the added mass coefficient for an infinite waving plate is given by (Coene 1992):

$$c_m = \frac{m_a}{\rho_f L} = \frac{2}{k}. \quad (4.11)$$

The added mass is thus a function of the non-dimensional wavenumber and dependent on the flapping mode. This is an important distinction from the cable problem, in which the added mass is estimated from the cable cross-section. The criterion for existence of flapping in the flag can now be rewritten in terms of the mode as

$$\frac{\mu}{\frac{1}{2}\mu k + 1} > 1.3Re^{-1/2} + K_B k^2. \quad (4.12)$$

Equation (4.12) shows the stabilizing effect of decreasing mass ratio (the left-hand side term decreases with decreasing μ), decreasing Reynolds number, and increasing bending rigidity. Recall that Zhang *et al.* (2000) and Zhu & Peskin (2002) found that increasing the length is destabilizing, an adjustment which increases Re and decreases K_B . These changes to Re and K_B are both destabilizing, and the observed trend comes from the combination of the effects.

Rearranging (4.12), we obtain the critical mass ratio

$$\mu = \frac{1.3Re^{-1/2} + K_B k^2}{1 - 0.65Re^{-1/2}k - 0.5K_B k^3}, \quad (4.13)$$

above which flapping will be realized. In cases where the mass ratio is small compared to the added mass, we find from (4.10) that this critical mass ratio reduces to

$$\mu = 1.3Re^{-1/2} + K_B k^2. \quad (4.14)$$

When bending rigidity can be neglected, the existence of flapping becomes a function of only the two parameters μ and Re , and flapping occurs above the critical mass ratio given by

$$\mu = 1.3Re^{-1/2}. \quad (4.15)$$

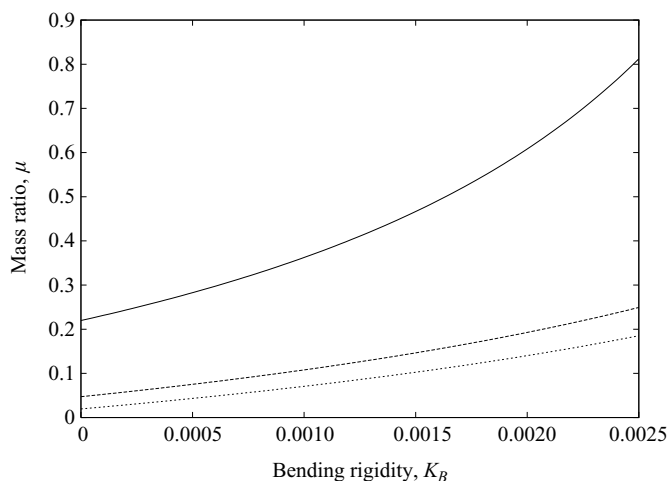


FIGURE 7. Critical mass ratio for flapping as a function of bending rigidity K_B for $Re = 100$ (—), $Re = 1000$ (— —), $Re = 5000$ (— · —), using (4.13) for the $k = 2\pi$ mode.

A plot of the stability relation (4.13) is shown in figure 7, depicting the relationship between the critical mass ratio μ and bending rigidity K_B for the $k = 2\pi$ mode at $Re = 100, 1000, 5000$. The plot shows the increased stability with lower Reynolds number and higher bending rigidity, with the intercepts at zero K_B representing the restoring influence of the viscous tension.

The linear analysis performed above would be more physically accurate if it were to include varying tension along the body, as well as the effect of global lift. A pin-ended thin body at an angle of attack will experience lift which tends toward flow alignment. A method for including this lift effect is laid out in the analysis of Argentina & Mahadevan (2005), but their approach has not yet been applied to the regime of interest in the present study. Rather than refining the linear analysis further, we continue the study using direct FSDS simulations which include the global lift wake effects and variable tension in the body.

4.2. Results using fluid-structure direct simulations (FSDS)

We use FSDS to investigate the fully nonlinear coupled dynamics of the flag flapping problem. Our objective is to elucidate the behaviour of the overall flapping dynamics and its dependence on the relevant non-dimensional parameters. Our regime of interest is in the limit of low bending rigidity (as would be the case of a cloth flag), where the viscous tension dominates the restoring force. As noted in §3.2, a finite value of bending rigidity must be used to ensure robustness of the structural numerical model, and a very low value of bending rigidity of $K_B = 0.0001$ is used in our simulations (the results are not sensitive to variation of K_B at this low value). In addition, we maintain essential inextensibility of the structure using $K_S = 10$.

Simulations are initiated with the body straight and at an angle of attack to the flow such that the initial non-dimensional tail amplitude is $A_0 = 0.1$. The initial flow condition is of a steady uniform flow with a small gradient buffer zone around the body used to minimize transients. As the simulation proceeds the body is initially displaced by the fluid-dynamic forcing toward alignment with the incoming flow, and it either settles to a stable-straight configuration, or experiences sustained flapping.

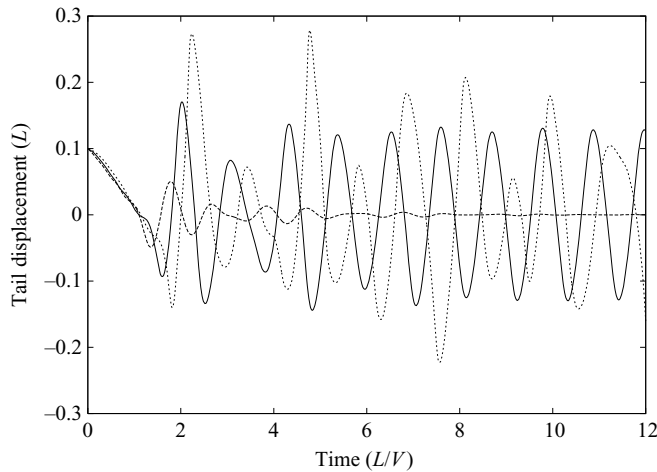


FIGURE 8. Time history of cross-stream tail displacement for regime (I) fixed-point stability with $\mu = 0.025$ (—); regime (II) limit-cycle flapping with $\mu = 0.1$ (---); and regime (III) chaotic flapping with $\mu = 0.2$ (····), with $Re = 1000$ and $K_B = 0.0001$.

We identify three distinct regimes of response (dependent on the value of the mass ratio μ): (I) fixed-point stability; (II) limit-cycle flapping; and (III) chaotic flapping. The differences in the response among the three regimes can be seen in figure 8, which plots the time history of the cross-stream displacement of the trailing edge or tail for one case from each response regime. In regime (I) the body settles to the steady straight configuration with no cross-stream displacement of the trailing edge, while in regime (II) the response settles to a period-one limit-cycle oscillation of constant frequency and amplitude. In regime (III) the trailing edge displacement exhibits sustained non-periodic behaviour characteristic of chaos.

For the case of $K_B = 0.0001$ and $Re = 1000$, we present in figure 9 the results from a series of simulations through a range of mass ratios of values of μ between 0.025 and 0.3, covering the three response regimes we mentioned. For each mass ratio value, we present four plots: a time history of the two-dimensional tail position for twenty non-dimensional time units; a phase plot of the cross-stream tail displacement against the cross-stream tail velocity; vorticity contours of the flapping wake for the fully developed flow; and a frequency plot displaying the normalized power spectrum for both the cross-stream tail displacement and the cross-stream flow velocity at a point two body lengths downstream of the equilibrium tail position.

For the regime (I) response for the value of $\mu = 0.025$ (figure 9a), the phase plot spirals in to a point, corresponding to the steady straight configuration, and the vortex wake represents a steady velocity-deficit wake. For the regime (II) response for $\mu = 0.05$ (figure 9b), the phase plot spirals to a limit-cycle trajectory, and the power spectrum exhibits a distinct frequency peak for the tail flapping. The corresponding limit-cycle vortex wake is the alternating vortex pattern of a von Kármán vortex street. The amplitude of the tail flapping and width of the vortex street increase with μ in regime (II) (figures 9b–9d), and the phase plane trajectories become larger while shifting slightly down in frequency. For $\mu = 0.125$ and higher (figures 9e–9j), the system enters regime (III), where the plot in the phase plane does not trend to a specific trajectory, the vortex wake becomes irregular, and multiple frequency peaks are seen in the power spectrum.

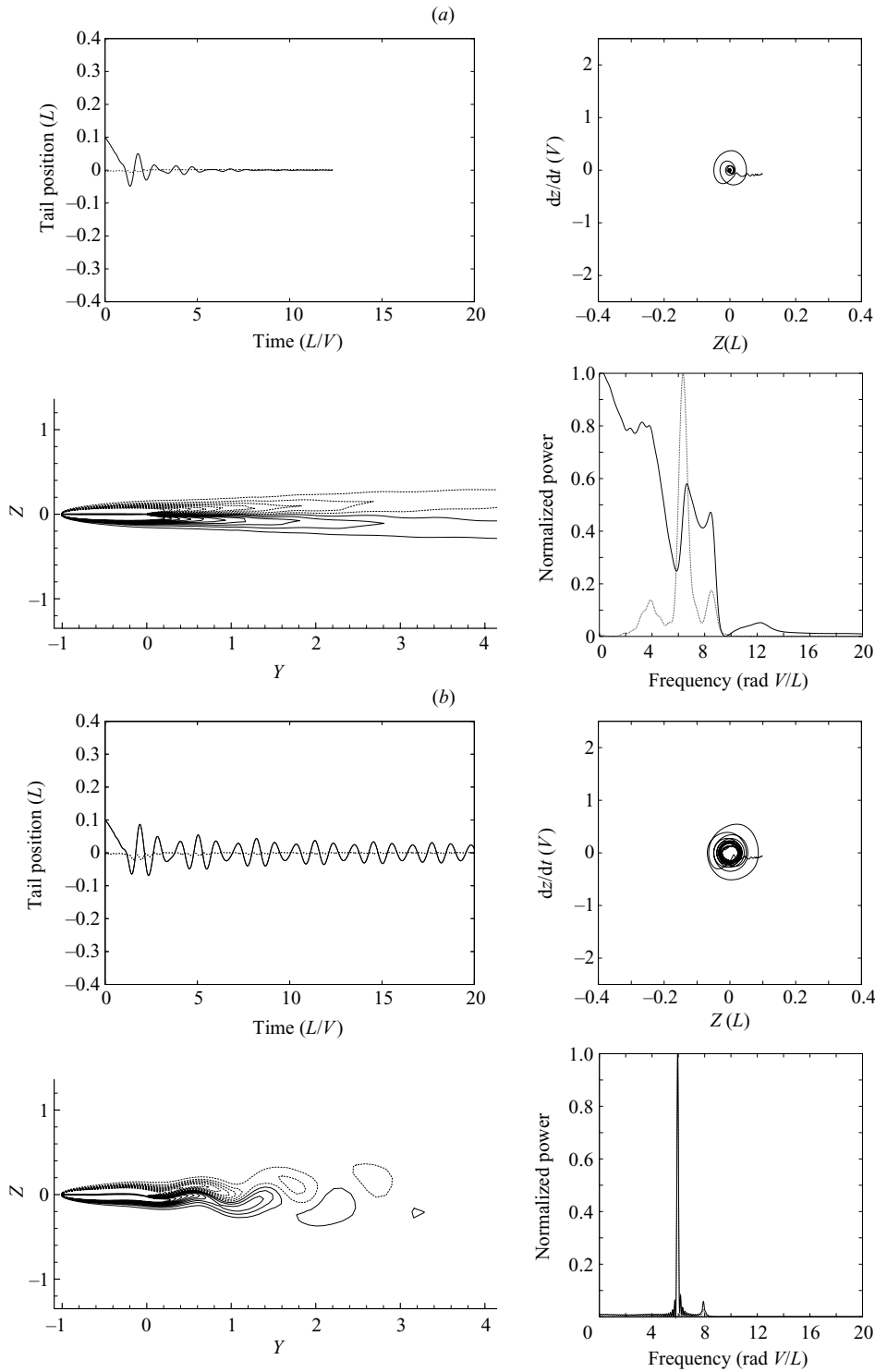


FIGURE 9. For caption see p. 52.

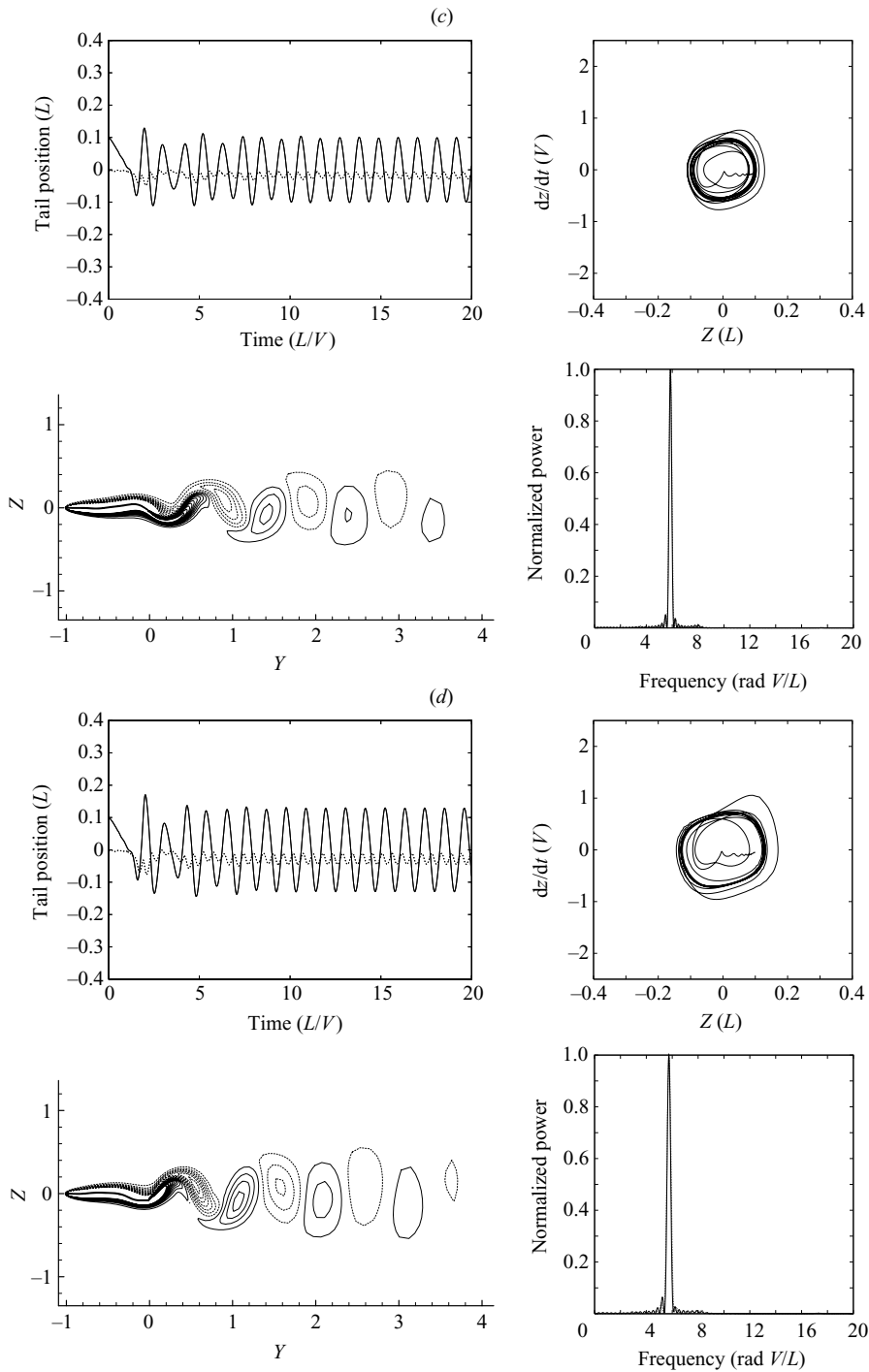


FIGURE 9. For caption see p. 52.

Trends of the response as a function of mass ratio μ are shown in figure 10. These include the tail amplitude taken as an average of the extrema, the value of the dominant frequency from the power spectra, the Strouhal number $St = f2A/V$,

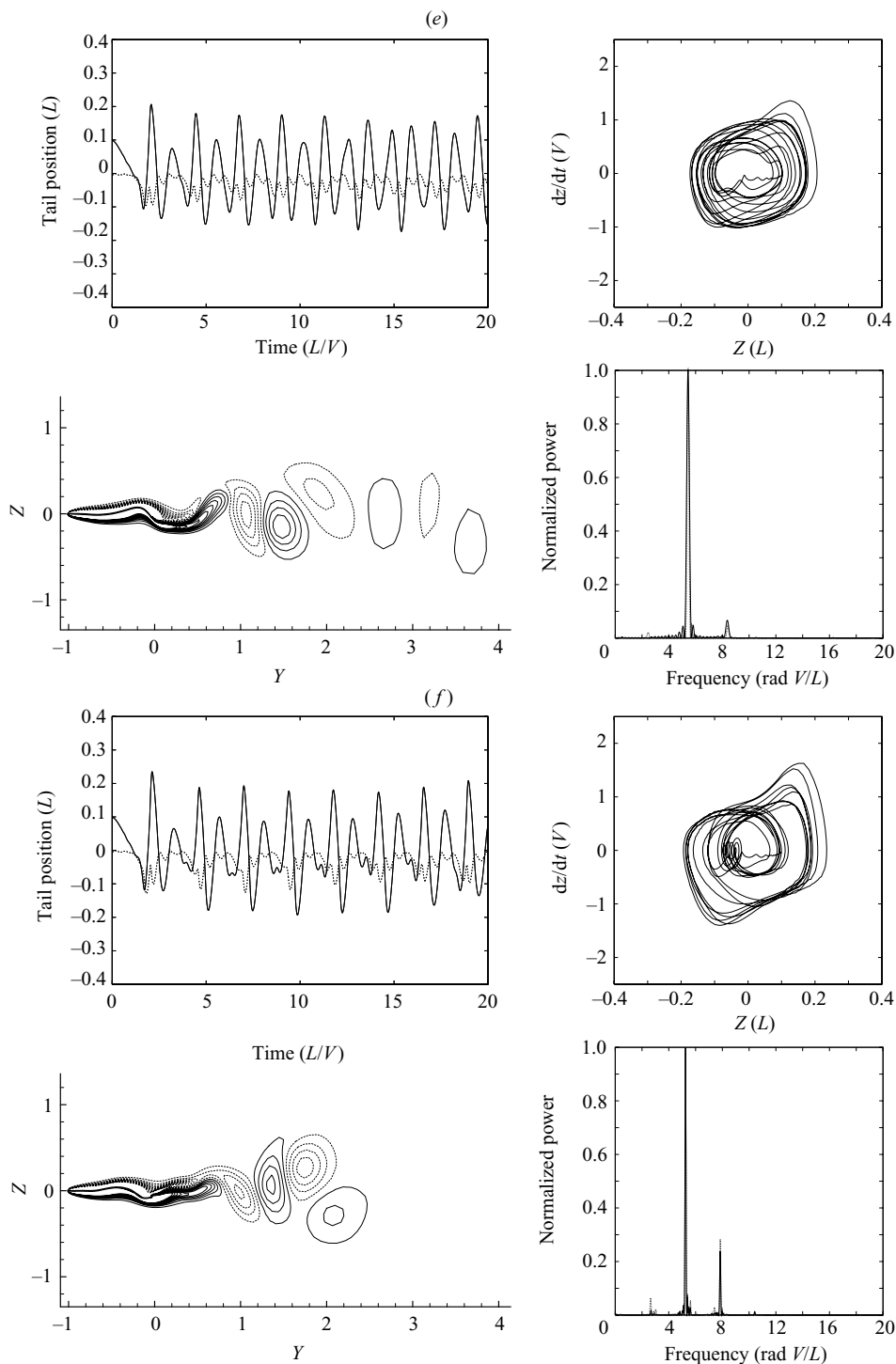


FIGURE 9. For caption see p. 52.

and the largest Lyapunov exponent calculated using the method of Wolf *et al.* (1985). If d measures the distance between two nearly identical states of the motion in the n -dimensional phase space, the largest Lyapunov exponent measuring the divergence

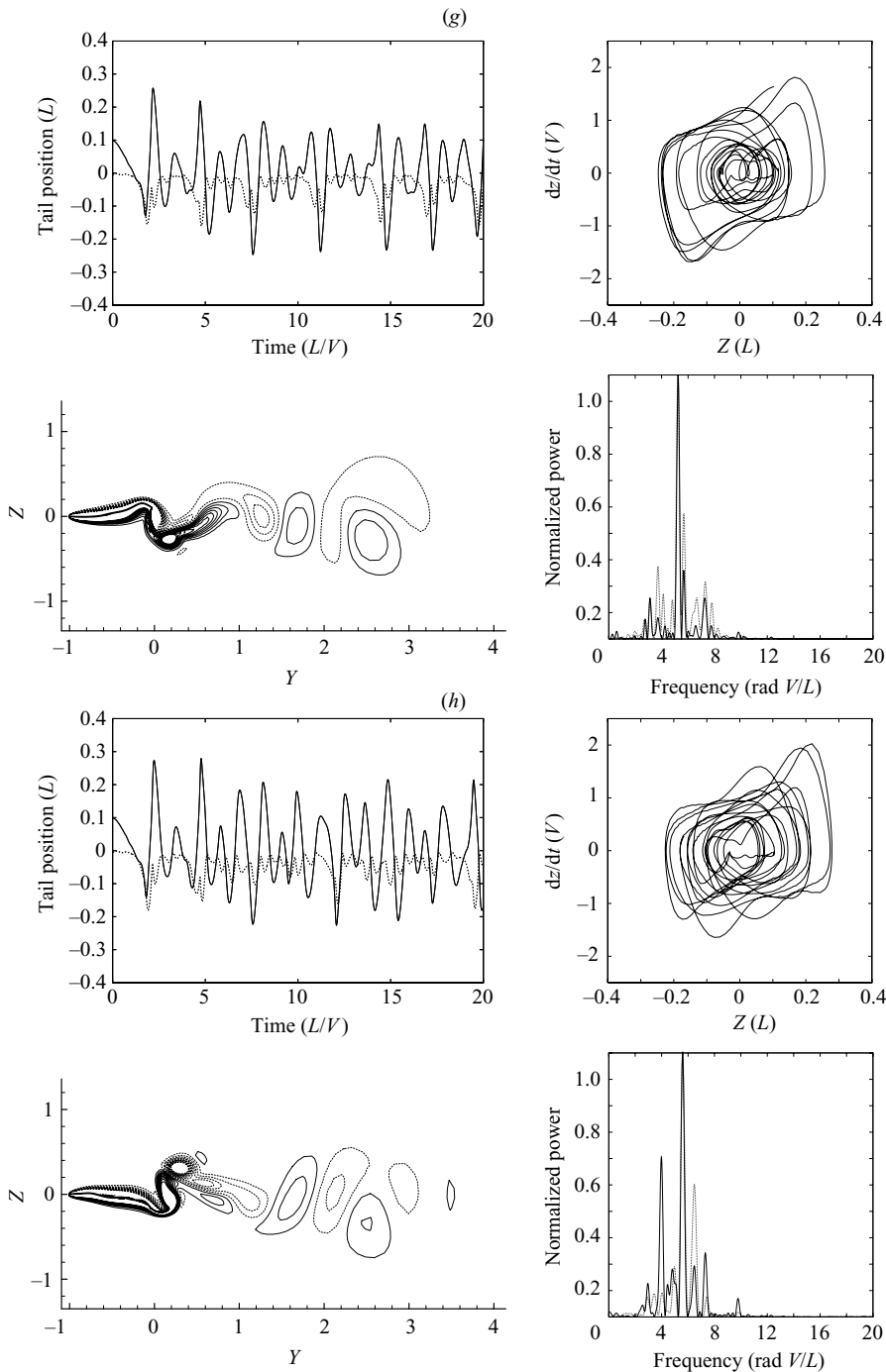


FIGURE 9. For caption see p. 52.

of nearby trajectories is estimated from the evolution of this distance, $d(t)$, by:

$$d(t) = d(t_0) e^{\lambda(t-t_0)}. \quad (4.16)$$

The value for d is approximated using the time history of the cross-stream tail displacement, and modelling the physics as a ten-dimensional system using the time delay

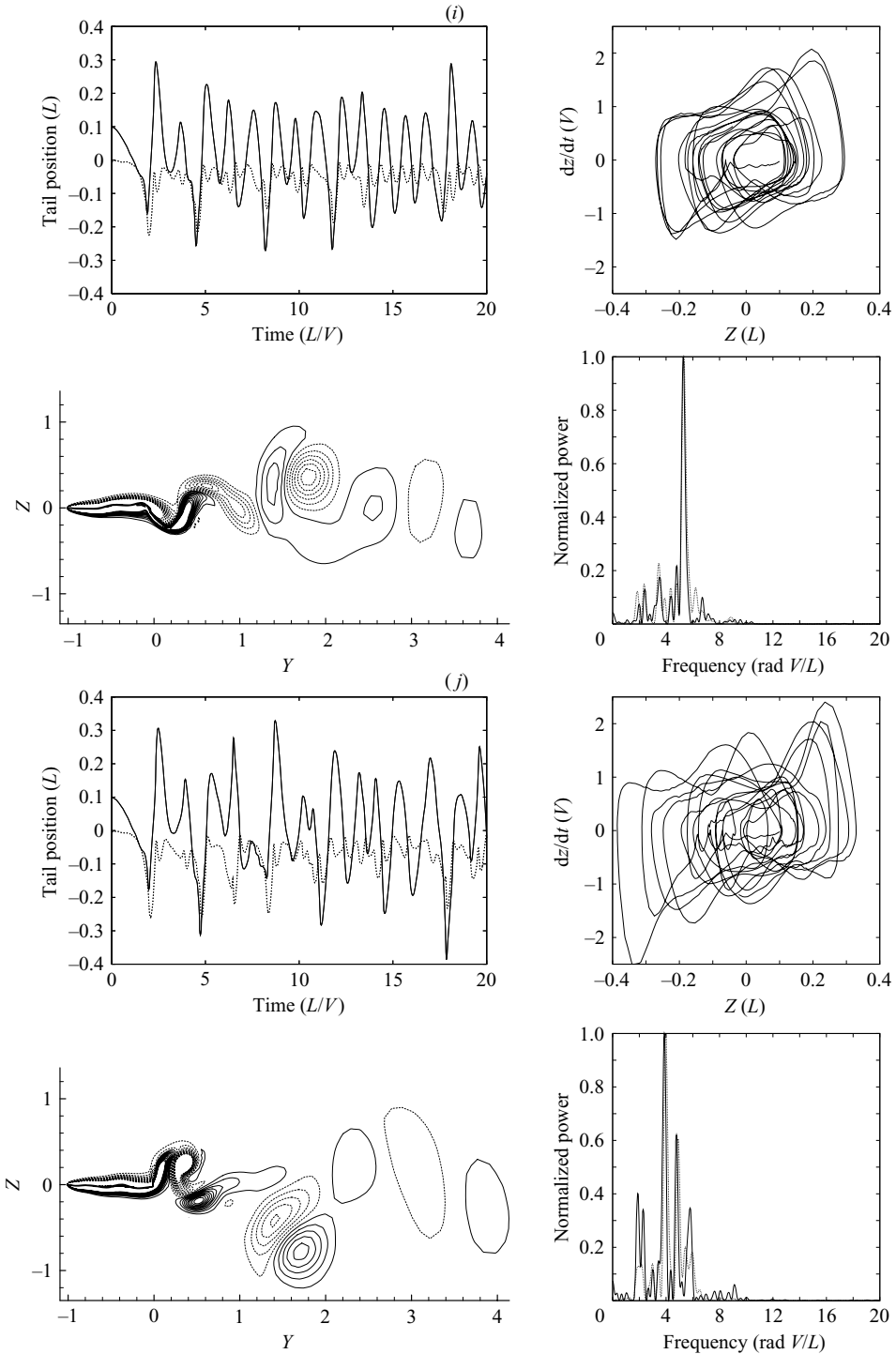


FIGURE 9. Time history of cross-stream (—) and streamwise (---) tail position; phase plot of cross-stream displacement and velocity; vorticity contours of the wake for fully developed flow; and frequency power spectrum of cross-stream displacement (—) and cross-stream velocity at the wake centreline $2L$ downstream from the equilibrium tail position (\cdots). Plotted for mass ratios of (a) $\mu = 0.025$, (b) $\mu = 0.05$, (c) $\mu = 0.075$, (d) $\mu = 0.1$, (e) $\mu = 0.125$, (f) $\mu = 0.15$, (g) $\mu = 0.175$, (h) $\mu = 0.2$, (i) $\mu = 0.25$, and (j) $\mu = 0.3$, with $Re = 1000$ and $K_B = 0.0001$.

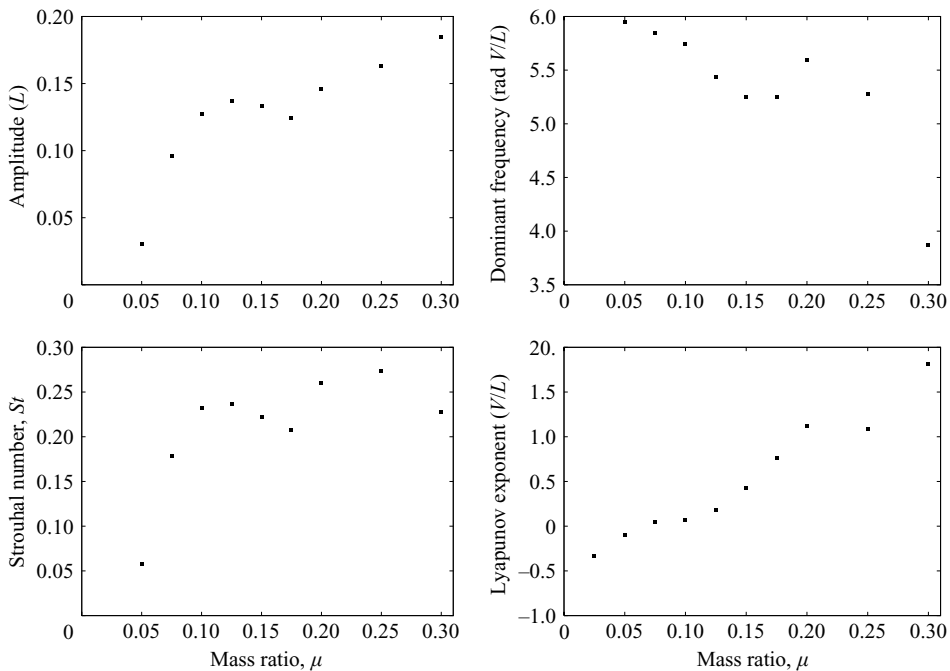


FIGURE 10. Flapping amplitude, frequency, Strouhal number, and largest Lyapunov exponent as a function of the mass ratio. All values are taken from the cross-stream tail displacement time series of figure 9, with $Re = 1000$ and $K_B = 0.0001$.

technique of Wolf *et al.* A negative value of λ indicates convergence, and positive value divergence, of nearly identical initial states.

We see in figure 10 that the flapping amplitude initially increases with mass ratio away from the critical point, levelling out at $A \simeq 0.15$; similar to the trend found away from stability in Watanabe *et al.* (2002). As the dominant frequency is reduced only slightly with increasing mass ratio, the Strouhal number follows a trend similar to the amplitude, levelling to a value between $St = 0.2$ and $St = 0.3$. The Lyapunov exponent, initially negative for the regime (I) point of $\mu = 0.025$, plateaus to zero for the regime (II) range of $\mu = 0.05 \rightarrow 0.1$, and takes on increasing positive values in regime (III) for $\mu = 0.125$ and above.

In the following, we discuss details of the fundamental mechanisms associated with this flapping response and regime transition. We relate the fixed-point stability to the linear analysis of §4.1 and consider the bistable phenomenon observed in prior studies. We also examine the features of the two unsteady flapping regimes and the mechanics of the transition from limit-cycle to chaotic flapping.

4.2.1. Fixed-point stability

The differences in initial evolution between the fixed-point stable mode and the flapping modes are shown in figure 11. The figure displays the body response at non-dimensional time intervals of 0.4 from $t = 0 \rightarrow 2$, as well as a vorticity contour plot at $t = 10$, for a case of fixed-point stability in figure 11(a) and a case of limit-cycle flapping in figure 11(b). The settling of the body into the flow-aligned configuration can be seen in the stable case, while continued oscillation around this configuration can be seen in the flapping case. The vorticity plot at $t = 10$ in the stable case indicates

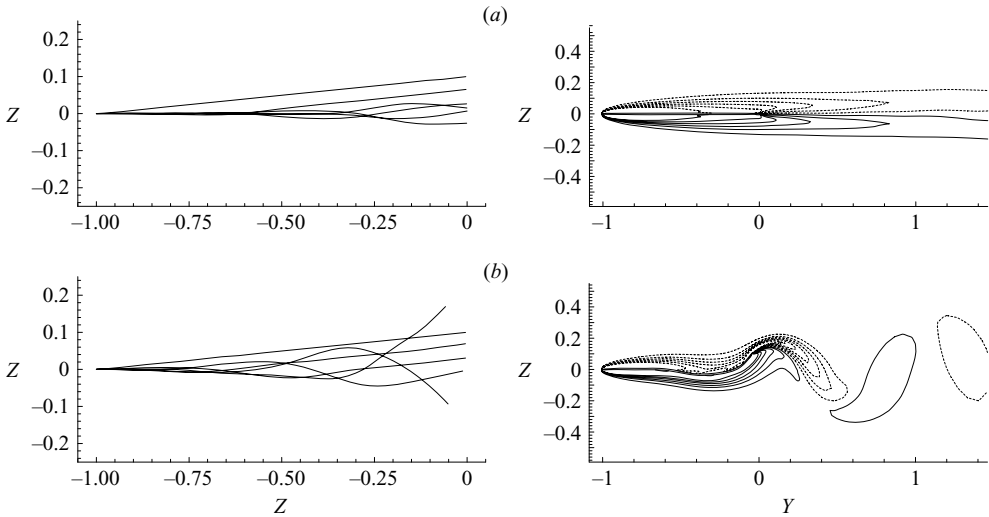


FIGURE 11. Body response at non-dimensional time intervals of 0.4 from $t=0 \rightarrow 2$ and vorticity plot at $t=10$ for (a) a fixed-point stable and (b) a flapping unstable case. Dashed lines indicate negative vorticity. Simulations for $Re=1000$ and $K_B=0.0001$ with (a) $\mu=0.025$ and (b) $\mu=0.1$.

a steady symmetric velocity-deficit wake, in contrast to the the unsteady vortex wake of the flapping case. It is this difference between sustained steady versus sustained unsteady evolution which defines whether the FSDS simulates a stable fixed point or an unstable flapping system.

A plot showing the FSDS flapping stability limit in $\mu-Re$ space for the low bending rigidity of $K_B=0.0001$ is given in figure 12(a). The stability limit of (4.15) is also plotted, showing good comparison between the two for the critical mass ratio. It is not surprising that the proportionality of (4.15) holds for stability. In the case of very low bending rigidity, the only two relevant parameters are the mass ratio μ and the Reynolds number Re . In seeking some natural relationship between these parameters, a new mass ratio can be considered which is scaled to the Blasius boundary layer thickness rather than the body length:

$$\tilde{\mu} = \frac{\rho h}{\rho_f L Re^{-1/2}} = \mu Re^{1/2}. \quad (4.17)$$

This modified mass ratio is the logical choice for a critical mass ratio which has Reynolds number dependence, and the numerical results of figure 12(a) confirm $\tilde{\mu}=1.3$ to be the critical value for the onset of flapping.

We now consider the effect of (small) bending rigidity, which we have predicted in (4.12) to be a function of the non-dimensional wavenumber. Considering $k=2\pi$, the wavelength being found close to the body length in Zhang *et al.* (2000), Watanabe *et al.* (2002), and the present simulations, we find the critical mass ratio for stability transition with bending rigidity to be predicted by

$$\mu_{crit} = 1.3 Re^{-1/2} + K_B 4\pi^2, \quad (4.18)$$

as plotted in figure 12(a). The very small difference in the stability curves excluding and including bending rigidity of figure 12(a) indicates that the bending rigidity at the low value of $K_B=0.0001$ has little influence on the stability. For the fixed Reynolds

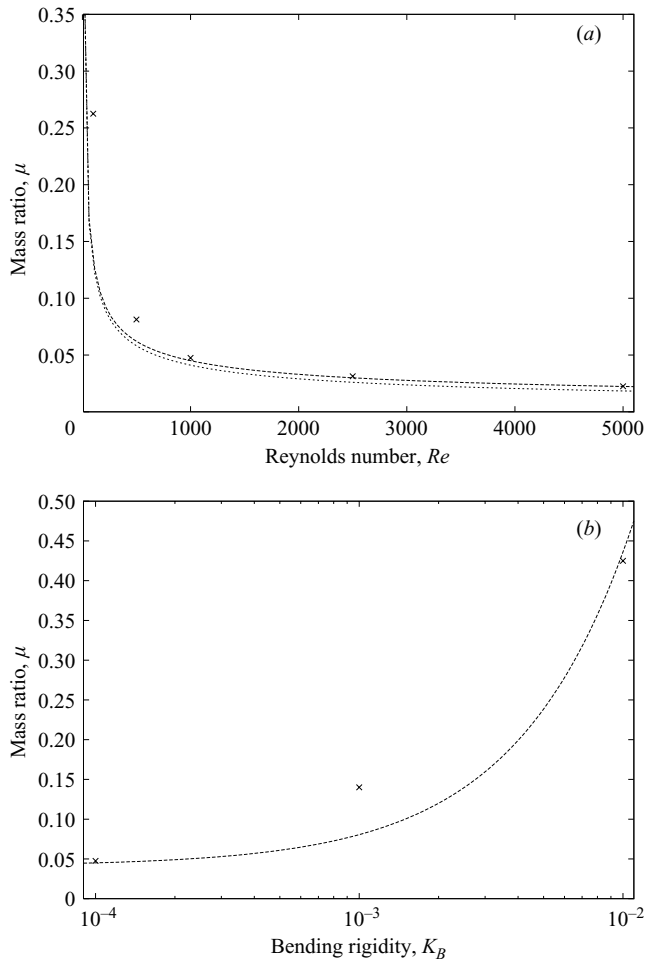


FIGURE 12. FSDS results for the critical mass ratio (\times), above which unstable flapping is realized. (a) For $K_B = 0.0001$ and a range of Reynolds numbers, plotted with (4.15) (---) and (4.18) (—). (b) For $Re = 1000$ and a range of bending rigidities, plotted with (4.18) (—).

number $Re = 1000$, we plot FSDS stability data for increasing bending rigidity in figure 12(b). The plot shows that the critical mass ratio given by (4.18) continues to be a good prediction for two orders of magnitude of higher rigidity.

Experimental data for stability transition from Watanabe *et al.* (2002) at $Re \sim 100\,000$ and from Shelley *et al.* (2005) at $Re \sim 50\,000$ were put in terms of K_B and μ for comparison to the present FSDS. We plot these experimental data with the FSDS data at $Re = 1000$ in figure 13. The trend of critical mass ratio with bending rigidity from FSDS is shown to follow that of the experimental data, but with a shift downward. As the prediction of (4.18) is for a higher critical mass ratio for these lower-Reynolds-number simulations, we look to the physics not modelled in the linear analysis for an explanation. The wake dynamics, which are not considered in the linear analysis, will be altered as the rate of dissipation of the shed vorticity will be less for the higher Reynolds numbers. Additionally, smaller-scale vortex structures will form at the higher Reynolds numbers. This effect was observed in the experiments of Zhang *et al.* (2000) at $Re = 20\,000$, but was not in the equivalent simulations of

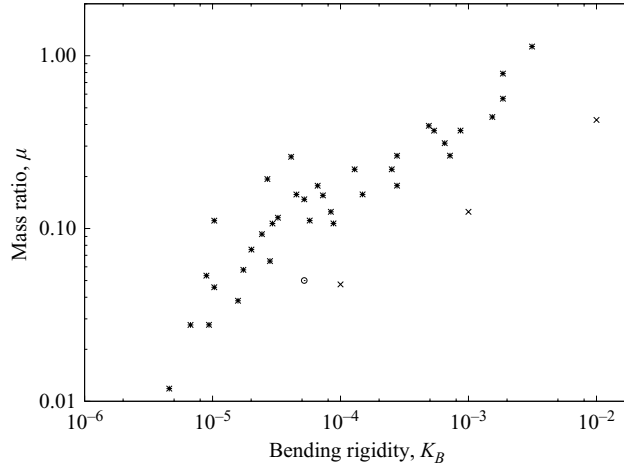


FIGURE 13. Mass ratio above which flapping is realized for a range of bending rigidities. Experimental results from Watanabe *et al.* (2002) (*) at $Re \sim 100\,000$, from Shelley *et al.* (2005) (○) at $Re \sim 50\,000$, and FSDS results (×) at $Re = 1000$.

Zhu & Peskin (2002) at $Re = 200$. Zhang *et al.* displays the periodic shedding of small-scale vortices in the wake while the body is in a non-flapping state. Such small-scale periodic shedding, which relieves the wake instability without body flapping, could account for the higher critical mass ratios of $Re \sim 10^5$ over $Re \sim 10^3$.

The influence of the relevant non-dimensional parameters on the physical effects relating to stability of the system are well predicted by the linear analysis of §4.1. The importance of the mass ratio on the appearance of the flapping instability is displayed. The question addressed in Shelley *et al.* (2005) of whether flapping will happen in the dense medium of water, is really just one of whether a sufficiently dense flexible material exists to obtain the necessary mass ratios. Varying the non-dimensional parameters, as we do in the present study, has a direct influence on the physical effects of the problem given by (4.7).

4.2.2. Subcritical bifurcation

The experiments of Zhang *et al.* (2000), Watanabe *et al.* (2002), and Shelley *et al.* (2005) at $Re \sim 10^4$ – 10^5 all observe subcritical bifurcation, a significant region of bistability where stable straight and unstable flapping modes can both be realized depending on the initial conditions. The phenomenon is also observed in the low-Reynolds-number numerical simulations of Zhu & Peskin (2002). For FSDS simulations at $Re = 1000$, we observe no significant region of bistability for $K_B = 0.0001$, while we do observe bistability for $K_B = 0.001$. For $\mu = 0.145$ we observe convergence to a sustained limit-cycle flapping state with amplitude $A = 0.05$ when the simulation is initiated with a tail displacement of $A_0 = 0.25$. However, when the simulation is initiated with a tail displacement of $A_0 = 0.001$, the body maintains this straight configuration, with no tendency to the flapping limit-cycle. Plots of the body position through several flapping cycles at $t \sim 40$ are shown in figure 14 for both the flapping and stable cases.

A common model to describe hysteresis in response is the Duffing equation, a forced mass–spring–dashpot system where the spring is nonlinear:

$$x_{tt} + bx_t + k(1 - \gamma x^2)x = F \cos(\omega t). \quad (4.19)$$

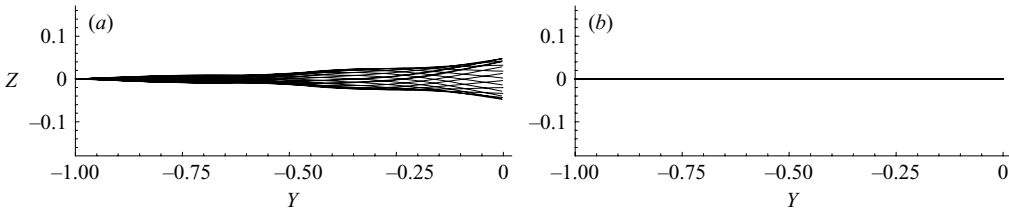


FIGURE 14. Body displacement through several flapping cycles at $t \sim 40$ with $K_B = 0.001$, $Re = 1000$, and $\mu = 0.145$, for initial conditions of (a) $A_0 = 0.25$ and (b) $A_0 = 0.001$.

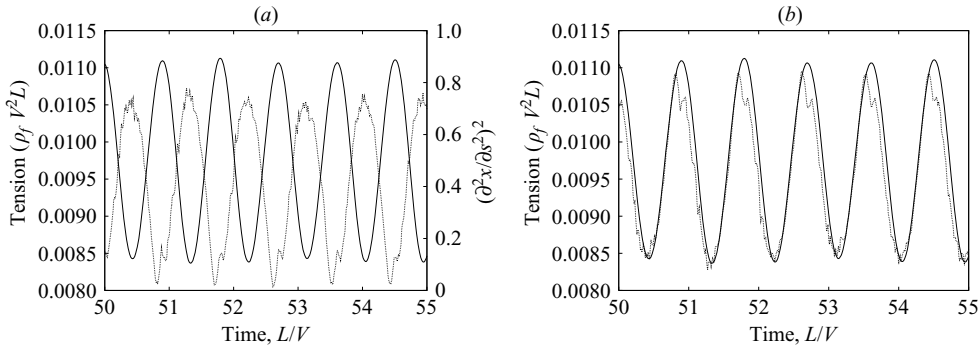


FIGURE 15. Time history of tension and body curvature at $s = 0.72$ for $K_B = 0.001$, $Re = 1000$, and $\mu = 0.145$, for the flapping case of $A_0 = 0.25$. (a) Measured tension (—), plotted with $(\partial^2 z / \partial y^2)^2$ (\cdots). (b) Measured tension (—), plotted with \tilde{T} (\cdots) of (4.21), using $T = 0.11$ and $\gamma = 0.32$.

For positive γ , the spring is softening, and amplitude hysteresis can be realized for forcing frequencies less than the natural frequency (see e.g. Drazin 1992). The analogous nonlinear restoring term for our flag analysis of §4.1 is

$$-T \left[1 - \gamma \left(\frac{\partial^2 z}{\partial y^2} \right)^2 \right] \frac{\partial^2 z}{\partial y^2}, \quad (4.20)$$

with a positive value of γ again indicating a softening spring. Defining \tilde{T} as

$$\tilde{T} = T \left[1 - \gamma \left(\frac{\partial^2 z}{\partial y^2} \right)^2 \right], \quad (4.21)$$

we consider this as a model for the measured value of the tension for the flapping case of $K_B = 0.001$ and $\mu = 0.145$. We plot together in figure 15(a) the FSDS time history of measured tension and $(\partial^2 z / \partial y^2)^2$, evaluated at $s = 0.72$, the position which experiences maximum curvature. The opposite phase of the two plots indicates that the tension decreases as the body curvature increases, and that γ has a positive value. We find a fit of \tilde{T} to the measured tension at $s = 0.72$ using $T = 0.11$ and $\gamma = 0.32$, as shown in the plot of figure 15(b). The flapping flag thus acts in the same manner as a softening spring in the Duffing equation, explaining the existence of hysteretic behaviour. While the higher-Reynolds-number experiments exhibit a much more significant bistable region than the present work, they also have considerably larger onset response amplitudes. The Duffing model predicts the existence and size of the hysteresis region to be similarly tied to the response amplitude through the magnitude of the external forcing.

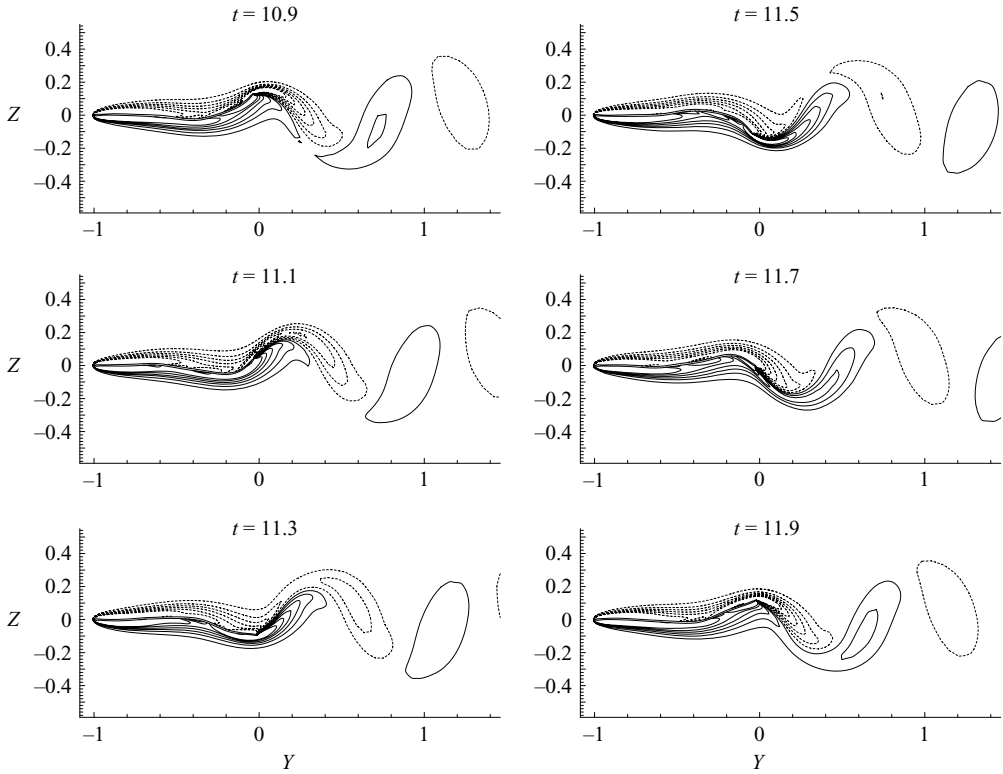


FIGURE 16. Time sequence of body position and associated vorticity contours for the response at $\mu = 0.1$ with $Re = 1000$ and $K_B = 0.0001$. Dashed lines indicate negative vorticity.

4.2.3. Limit-cycle flapping

The limit-cycle flapping of regime (II) is marked by the convergence of the flapping to a single-frequency oscillation which exactly repeats itself. The corresponding phase plots in figures 9(b)–(9d) trace out a single-loop closed line when the flapping is converged. A sequence of plots for the regime (II) case of $\mu = 0.1$, showing the body flapping and contours of vorticity in the fluid, is given in figure 16. The response is of a travelling wave of increasing amplitude from leading edge to trailing edge, as was observed in previous studies. The strong vorticity spinning off the tail when it is at maximum displacement is shed as a discrete vortex in the wake as the tail sweeps back through the zero point. This process is repeated in symmetry as the tail passes through maximum displacement in the opposite direction. A von Kármán vortex street, consisting of a continuous series of alternately signed vortices, is the resulting wake. The wake plots of figure 9 show that for increasing mass ratio in the limit-cycle regime, these wake vortices become elongated in the cross-stream direction as the Strouhal number increases.

As we are looking at a limit of very low bending rigidity and very high extensional rigidity, there is limited participation of structural potential energy in the energy budget. Thus, the oscillation consists primarily of an exchange of energy between the total kinetic energy (fluid and structure) and the fluid potential energy in the form of the pressure gradient driving the flow. To examine this, we decompose the kinetic and potential energies to isolate the oscillating components. The oscillating

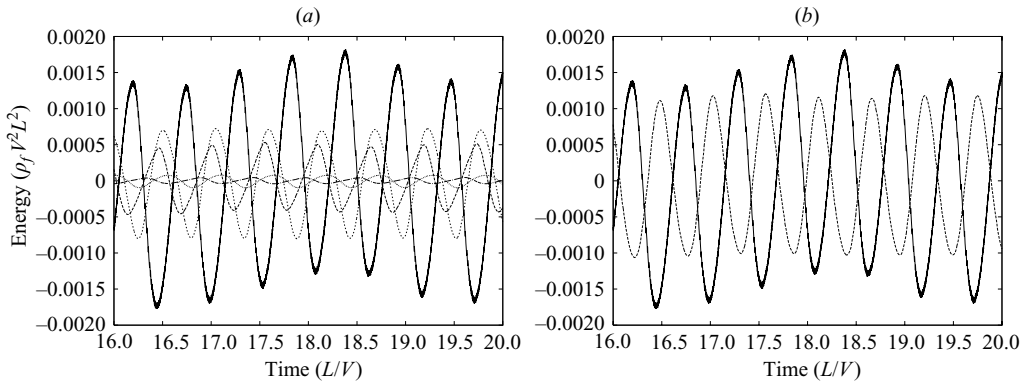


FIGURE 17. Time history of the oscillating part of the energy components for $\mu = 0.1$ with $Re = 1000$ and $K_B = 0.0001$, from $t = 16 \rightarrow 20$. (a) Plot of fluid-potential (—), fluid-kinetic (---), structural-kinetic (- · - · -), structural-bending potential (·····), and structural-stretching potential (— · —) energies. (b) Plot of fluid-potential (—), and total kinetic (---) energies.

energy components for the $\mu = 0.1$ case are plotted in figure 17(a) from $t = 16 \rightarrow 20$, near limit-cycle convergence. The plot shows very little participation of the structural potential energy, with the majority of the energy exchange being between the fluid-potential energy and the fluid- and structural-kinetic energy. The sum of the kinetic energies is plotted with the fluid potential energy in figure 17(b), showing the near balance in the magnitude of the oscillation. The minimal participation of the structural potential energies is a reflection of the bending and extensional rigidities approaching their infinitesimal and infinite limits, respectively, where the actual values of these parameters do not significantly influence the system evolution.

4.2.4. Transition to chaos

Figure 9 reveals that the period-one limit-cycle flapping is broken up as the mass ratio goes to $\mu = 0.125$ and higher. We see from figure 10 that this corresponds to a Strouhal number of $St = 0.23$. This corresponds to the natural frequency of the fluid dynamics defined by a universal Strouhal number of $St = 2Af/V \simeq 0.2$ (e.g. Sarpkaya 1979). Thus, the transition to chaos occurs when the flag flapping frequency is in the neighbourhood of the natural wake frequency. Changes in the behaviour of nonlinear systems near resonance overlap is a common phenomenon (e.g. Olson & Olsson 1991), and an example close to the present context is the distinct nonlinear behaviour of vortex-induced vibration of flexible cylinders when the structural natural frequency approaches the wake frequency (Sarpkaya 1979; Williamson & Govardhan 2004).

A common path in the transition from a period-one limit cycle to chaos in nonlinear systems is successive period doubling (e.g. Procaccia 1988; Olson & Olsson 1991), which would initially show up as a signal at $1/2$ of the dominant limit-cycle frequency. What we observe, however, at $\mu = 0.125$ and $\mu = 0.15$, is the appearance of a second significant frequency component with a value of $3/2$ that of the dominant frequency. The signal is period-two periodic but without a significant component at the period-two frequency (as $\sin((2\pi/T)t) + \sin((3\pi/T)t)$ is periodic in $2T$). As soon as the limit cycle is broken, for $\mu > 0.1$, the largest Lyapunov exponent takes on a positive value. This indicates transition from a period-one limit cycle to a chaotic system directly or in a very narrow transition region.

Defining the dominant limit-cycle frequency as ω_L , the appearance of the second frequency component at $3\omega_L/2$ suggests a nonlinear combination of the dominant

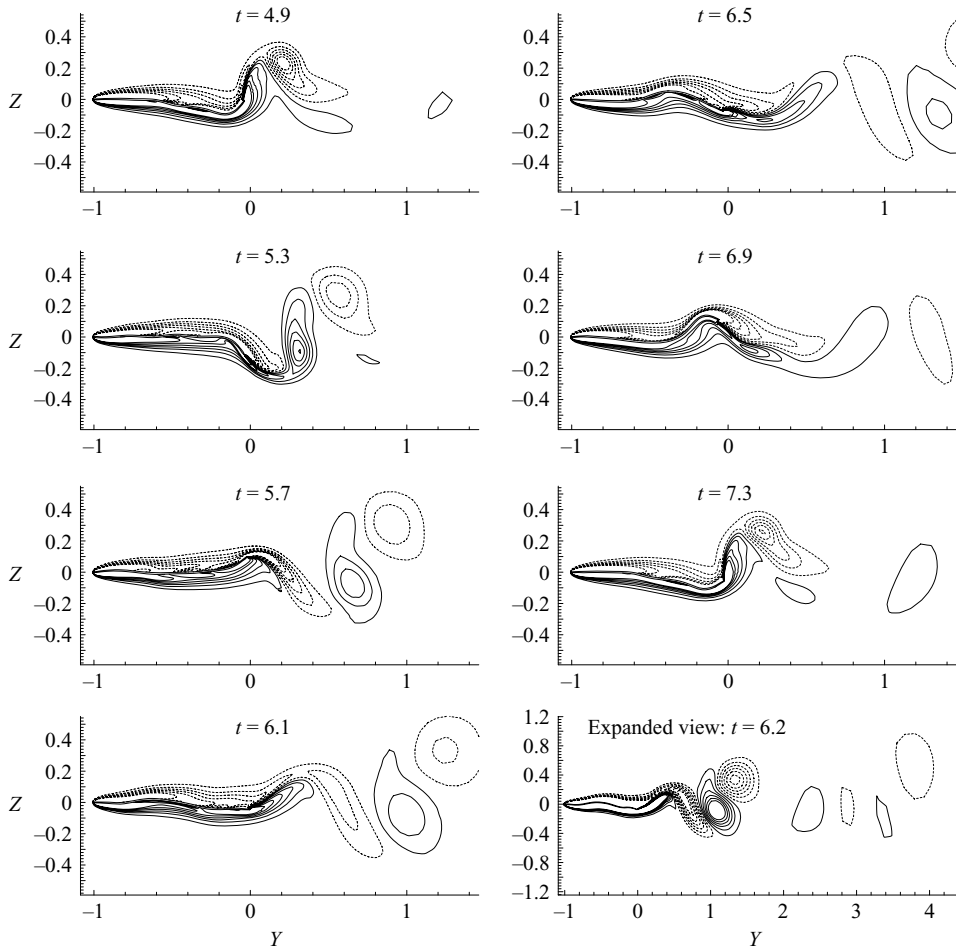


FIGURE 18. Time sequence of body position and associated vorticity contours for the response at $\mu = 0.15$ with $Re = 1000$ and $K_B = 0.0001$. Dashed lines indicate negative vorticity. The final frame is an expanded view using higher-resolution vorticity contours.

frequency with the period-doubled frequency of $\omega_L/2$. A constraint on the realization of the $\omega_L/2$ subharmonic could be effecting an immediate transfer of that energy to the $3\omega_L/2$ component. It has been well established that there exist specific wake modes which represent stable patterns of vortex distribution into the wake. These are covered in detail in Williamson & Roshko (1988), where the specific case of the $\omega_L/2$ subharmonic mode is addressed, and it is argued that lack of symmetry precludes it from being a natural mode.

With all of the cases for $\mu > 0.1$, with the $3\omega_L/2$ superharmonic being Lyapunov unstable, the system tends to this chaotic attractor. We now consider the vortex wake associated with this mode. The case for $\mu = 0.15$, with the strong superharmonic, is examined between the period-two cycle of $t = 4.9 \rightarrow 7.3$. The three peaks through the two-cycle can be seen in the $\mu = 0.15$ time series plot, along with a triple-loop in the corresponding phase plot. Figure 18 gives a sequence of plots showing the body flapping and vorticity contours. While the vortex pattern is not symmetric, it is notable that the hesitation, or small tail wiggle, at $t = 6.5$ creates a dead zone in

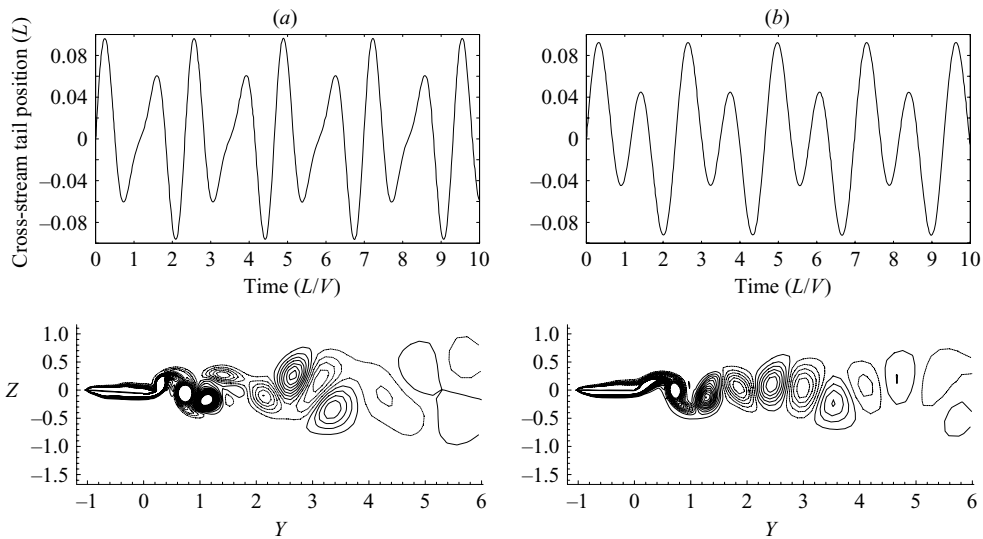


FIGURE 19. The upper plots are the time history of cross-stream tail displacement for the rigid foil forced in (a) the $3/2$ superharmonic mode $A \sin(\omega t) + 0.5A \sin(1.5\omega t)$ and (b) the $1/2$ subharmonic mode $A \sin(\omega t) + 0.5A \sin(0.5\omega t)$. The lower plots are the corresponding vortex wake at $t = 10$, with dashed lines representing negative vorticity.

the vortex wake. The result is a separation between vortex clusters in the wake, a phenomenon that can be seen in the expanded view of the final frame in figure 18. Flapping with the dominant frequency and $\omega_L/2$ subharmonic would have a more even distribution of the vortices in an asymmetric wake, and the system avoids such a mode.

The differences between the wakes with the $3\omega_L/2$ harmonic versus the $\omega_L/2$ harmonic are examined by forcing the body to oscillate (as a straight rigid foil) in these two modes. The signals used are $A \sin(\omega t) + 0.5A \sin(1.5\omega t)$ and $A \sin(\omega t) + 0.5A \sin(0.5\omega t)$. The time history of the tail displacement and the vortex wake at the end of the simulation, at $t = 10$, are given in figure 19. The plot of the $3/2$ superharmonic mode shows vortex clustering in the wake. A series of three strong vortices (positive-negative-positive) is shed in a diagonal formation, separated by a region of weaker negative vorticity. The $1/2$ subharmonic mode, on the other hand, shows evenly spaced alternating vortices with three shed in the upper part of the wake followed by one shed in the lower part of the wake. While the construction of these forced $3/2$ superharmonic and $1/2$ subharmonic modes is somewhat arbitrary, they do display the anticipated differences. The indication is that wake clustering is the preferred mode to the asymmetric evenly spaced pattern, and thus the period-doubled energy of the flapping flag feeds into the $3/2$ superharmonic.

4.2.5. Snapping

As we see in the the power spectrum plots of figures 9(g)–9(j), mass ratio values of $\mu = 0.175$ and above result in broadband responses. Associated with this are further increases in the Lyapunov exponent, and a noticeably less regular time series and phase plot. The time series for these larger values of mass ratio indicate intermittent large and violent (indicated by the rapid change in direction) snapping events interspersed among smaller oscillations. This type of chaotic behaviour associated with snapping has been described in other contexts, for example, in the case of a moored near-surface

Mass ratio, μ	Number of snapping events	Lyapunov exponent, λ	Regime
0.1	0	0.07	(II)
0.125	0	0.18	(III)
0.15	0	0.42	(III)
0.175	1	0.76	(III)
0.2	2	1.12	(III)
0.25	4	1.09	(III)
0.3	6	1.81	(III)

TABLE 1. Number of snapping events for each mass ratio from $t=0 \rightarrow 20$, listed with the largest Lyapunov exponent and the identified motion regime, for $Re=1000$ and $K_B=0.0001$.

body (Zhu *et al.* 1999). It is also commonly observed in everyday chaotic flapping of flag-like bodies.

‘Snapping’ connotes a rapid acceleration, and, for the purpose of this study, we define a snapping event as a spike in the magnitude of the trailing edge acceleration which exceeds $30V^2/L$. Using this definition, the number of snapping events over a simulation time of 20 convective units is given in table 1 for the mass ratios $\mu=0.1 \rightarrow 0.3$, with $Re=1000$ and $K_B=0.0001$. From the data, we see there is absence of snapping in the limit-cycle regime and for low mass ratio ($\mu \lesssim 0.15$) cases of regime (III). Beyond the threshold value of $\mu \approx 0.15$, the frequency of snapping increases appreciably with increasing μ , as does the largest Lyapunov exponent.

The kinematics, dynamics, and flow vorticity associated with snapping and recovery is elucidated by examining in detail a single snapping event. The time history of the body drag for the chaotic case of $\mu=0.3$ is given in figure 20(a), displaying a number of strong peaks in the drag force which correspond to snapping events. As an illustration, we consider the event occurring at $t \simeq 18$ and thus focus on the dynamics of the system encompassing this event from $t=17 \rightarrow 19$. The fluid-dynamic drag effect to the body is plotted in figure 20(b), the kinematics of the body is displayed in the series of displacement plots of figure 21, and the vorticity evolution in the near wake is plotted in figure 22. We examine points in time corresponding to different stages in the evolution of the snapping event: time *A* at $t=17.6$, just prior to snapping; time *B* at $t=17.9$, at the end of snap-through; time *C* at $t=18.2$, during recoil; and time *D* at $t=18.5$, at the completion of the snapping event.

The plots of the body displacement show a large wave travelling down the body, creating a hook in the tail at time *A*. Associated with this hook at the tail, a strong positive vortex begins to develop at the underside of the body. After time *A* the tail begins to snap, and there is a rapid increase in the drag on the body which peaks during the snap-through, just prior to time *B*. The vorticity plot at time *B* shows that the strong positive vortex that has developed on the underside of the body is shed as a very strong vortex displaced far from the wake centreline. While this positive vortex in the lower half of the wake is a drag vortex, the subsequent upsweep of the tail between times *B* and *C* creates a negative vortex in the lower half of the wake, which is associated with thrust. The drag history reflects this generation of thrust, with a minimum negative value to the drag at time *C*.

The loss of tension in the body associated with the thrust at time *C* marks the initiation of a dynamic buckling of the body. Such buckling is seen in the displacement plots beginning, at time *C*, as a spontaneous appearance of a high wavenumber mode shape which is essentially stationary for a short period of time, before rolling out to

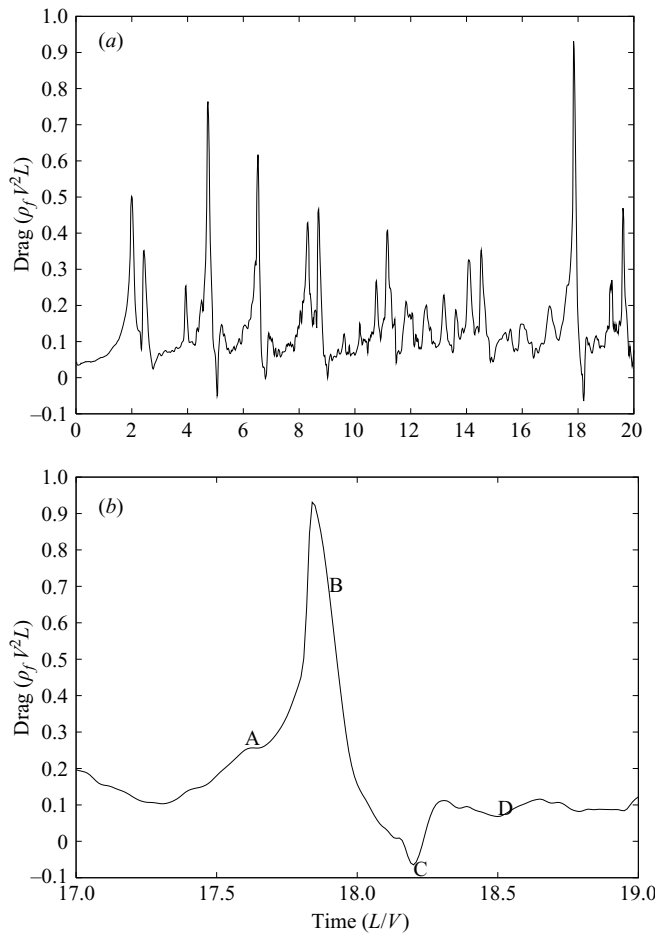


FIGURE 20. Time history of the drag for $\mu = 0.3$ with $Re = 1000$ and $K_B = 0.0001$, as measured by the total fluid-dynamic forcing on the body in the streamwise direction. (a) Drag history for the entire simulation, and (b) drag history showing detail of the snapping event at $t \approx 18$ with time points A, B, C, and D indicated.

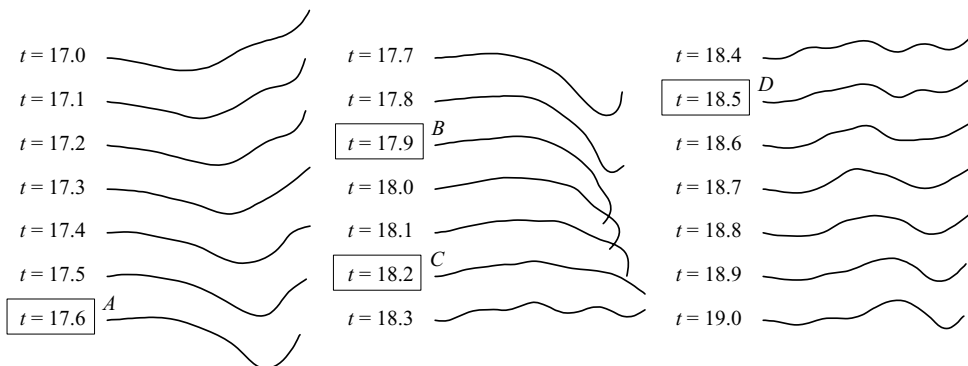


FIGURE 21. Time sequence of body position for $\mu = 0.3$ with $Re = 1000$ and $K_B = 0.0001$, with time points A, B, C, and D indicated.

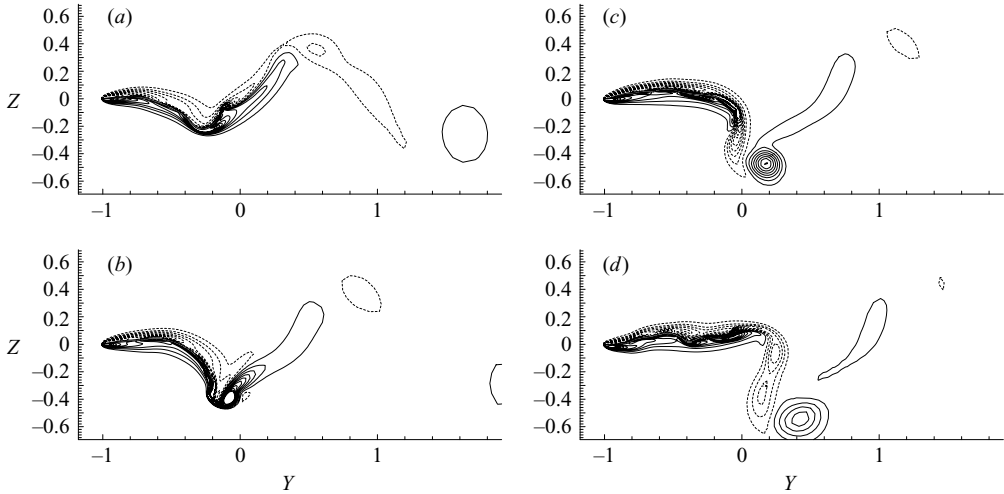


FIGURE 22. Vorticity contours in the wake at (a) time A, $t = 17.6$, (b) time B, $t = 17.9$, (c) time C, $t = 18.2$, and (d) time B, $t = 18.5$, for $\mu = 0.3$ with $Re = 1000$ and $K_B = 0.0001$. Dashed lines indicate negative vorticity.

the tail as a travelling wave beginning at time D . The rapid change in body tension, loss of positive tension, and associated high mode buckling are characteristic of the cable snapping problem, as described in Zhu *et al.* (1999).

Time D represents the completion of the snapping event, as the fluid-dynamic drag returns to a consistent positive value and the body displacement no longer exhibits dynamic buckling. Thus the vortex wake at D provides the completed picture of a wake associated with a snapping event. With the strong positive and negative vortices being shed in the lower half of the wake, there is a resultant vortex dipole displaced well below the wake centreline which continues to migrate downward. Thus the violent snapping events in the chaotic regime are characterized by the associated rapid variation in the fluid-dynamic forcing and internal tension, as well as distribution of high-strength vortices away from the wake centreline.

4.2.6. Regime map

The stability and response results for the low bending rigidity case we consider can be summarized in the diagram of figure 23 on the $Re - \mu$ plane. While we have considered a large number of mass ratio cases for the detailed investigation at $Re = 1000$, we performed select runs at higher and lower Reynolds numbers that help complete the picture of the trends in response transition. The figure shows the three response regimes of (I) fixed-point stability, (II) limit-cycle flapping, and (III) chaotic flapping. The curve of transition from stable to limit-cycle response is plotted as μ_{crit} from (4.18). For transition to chaos, we find that a reasonable fit of the critical mass ratio values for that transition is given by

$$\mu_{\text{chaos}} = 2.5\mu_{\text{crit}} = 3.25Re^{-1/2} + K_B 10\pi^2. \quad (4.22)$$

These transition curves of (4.18) and (4.22) fit the data well for all but the lowest Reynolds number, $Re = 100$, where the critical mass ratio for transition to limit-cycle flapping is underpredicted, and no chaotic response was found with FSDS up through $\mu = 0.5$. The changes associated with regime transition with increasing mass ratio are indicated in figure 23, including the vortex wake patterns and value of the largest

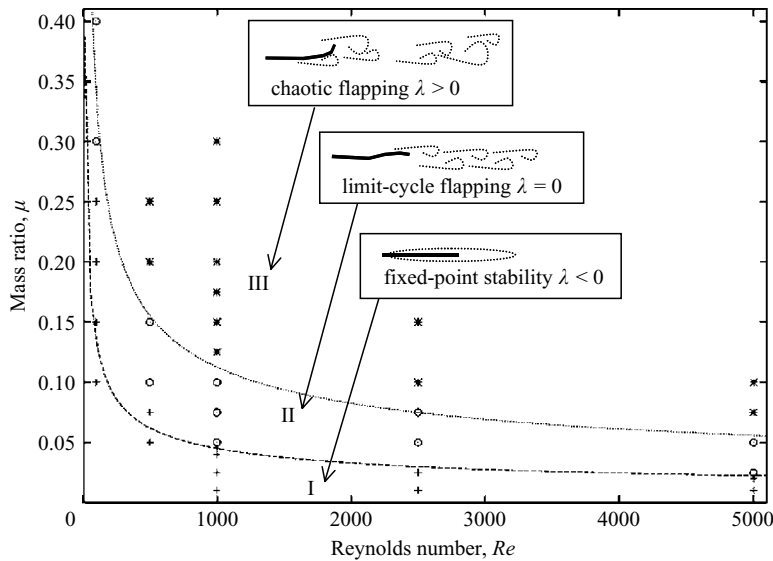


FIGURE 23. Bifurcation diagram for $K_B = 0.0001$ shows the fixed-point stability limit given by (4.18) (—), and the curve indicating transition from limit cycle to chaotic response given by (4.22) (·····); with FSDS data indicating the response regime as (I) fixed-point stability (+); (II) limit-cycle flapping (○); or (III) chaotic flapping (*). Wake patterns and the sign of the largest Lyapunov exponent are indicated for each response regime.

Lyapunov exponent. As the mass ratio is increased, the velocity-deficit wake of the fixed point becomes a limit-cycle alternating vortex pattern of the von Kármán wake. Increasing the mass ratio further, into the chaotic regime, the wake is characterized by non-periodic vortex clustering. The value of the largest Lyapunov exponent indicates the response regime: negative for stable fixed point, zero for limit cycle, and positive for chaotic flapping.

5. Conclusions

We consider the problem of the flapping motion of a thin flexible body in a uniform flow. For low extensibility and bending stiffness of the body, the problem is controlled by the non-dimensional parameters of Reynolds number $Re = VL/\nu$ and mass ratio $\mu = \rho_s h / (\rho_f L)$. A linear analysis indicates the destabilizing effect of higher mass ratio and Reynolds number (and the stabilizing effect of higher bending rigidity $K_B = EI / (\rho_f V^2 L^3)$).

We develop a direct simulation of the fully nonlinear coupled fluid-structure problem. The predictions of the linear stability analysis are confirmed by our direct numerical simulations and we suggest (4.18) as a good prediction of the critical mass ratio, above which flapping will be realized.

Running the fluid-structure direct simulations (FSDS), we obtain a systematic set of results for select Reynolds numbers over a broad range of mass ratios. As the mass ratio is increased, the results reveal three distinct regimes of response summarized in figure 23. These are defined by (I) fixed-point stability, (II) limit-cycle flapping, and (III) chaotic flapping. As μ increases above the first (flapping) critical value, the response transitions from a stable fixed point to a travelling-wave flapping limit cycle. This period-one limit cycle increases in amplitude with mass ratio (with a slight

decrease in the flapping frequency), until the Strouhal number of the system reaches the value of the natural wake frequency. As μ is increased beyond this second (chaos) critical value, the motion undergoes a direct transition from a period-one limit cycle to chaos. The breaking up of the limit cycle emerges as a $3/2$ superharmonic of the limit-cycle frequency (the period-doubled $1/2$ subharmonic does not represent a natural wake frequency). This chaotic motion is measured by a positive value of the largest Lyapunov exponent, which increases with increasing mass ratio. As μ increases further, the eventual broadband response is characterized by irregular flapping motion with intermittent violent snapping events accompanied by large rapid changes in tension, dynamic buckling, and shedding of strong vortices away from the wake centreline.

REFERENCES

- ALLEN, J. J. & SMITS, A. J. 2001 Energy harvesting eel. *J. Fluids Struct.* **15**, 629–640.
- ARGENTINA, M. & MAHADEVAN, L. 2005 Fluid-flow-induced flutter of a flag. *Proc. Natl Acad. Sci.* **102**, 1829–1834.
- ARMFIELD, S. W. 1991 Finite difference solutions of the Navier–Stokes equations on staggered and non-staggered grids. *Comput. & Fluids* **20**, 1–17.
- CHORIN, A. J. 1968 Numerical solution of the Navier–Stokes equations. *Math. Comp.* **22**, 745–762.
- COENE, R. 1992 Flutter of slender bodies under axial stress. *Appl. Sci. Res.* **49**, 175–187.
- CONNELL, B. S. H. 2006 Numerical investigation of the flow-body interaction of thin flexible foils and ambient flow. PhD thesis, Massachusetts Institute of Technology, Cambridge, MA.
- DICKINSON, M. H. & GOTZ, K. G. 1993 Unsteady aerodynamic performance of model wings at low Reynolds numbers. *J. Expl Biol.* **174**, 45–64.
- DRAZIN, P. G. 1992 *Nonlinear Systems*, chap. 7. Cambridge University Press.
- DUTSCH, H., DURST, F., BECKER, S. & LIENHART, H. 1998 Low-Reynolds-number flow around an oscillating circular cylinder at low Keulegan–Carpenter numbers. *J. Fluid Mech.* **360**, 249–271.
- FARNELL, D. J. J., DAVID, T. & BARTON, D. C. 2004a Coupled states of flapping flags. *J. Fluids Struct.* **19**, 29–36.
- FARNELL, D. J. J., DAVID, T. & BARTON, D. C. 2004b Numerical simulations of a filament in a flowing soap film. *Intl J. Numer. Meth. Fluids* **44**, 313–330.
- GOBAT, J. I., GROSENBAUGH, M. A. & TRIANTAFYLLOU, M. S. 2002 Generalized- α time integration solutions for hanging chain dynamics. *J. Engng Mech.* **128**, 677–687.
- GRAY, J. 1933 Studies in animal locomotion. I. The movement of fish with special reference to the eel. *J. Expl Biol.* **10**, 88–104.
- HOWELL, C. T. & TRIANTAFYLLOU, M. S. 1993 Stable and unstable nonlinear resonant response of hanging chains: Theory and experiment. *Proc. R. Soc. Lond. A* **440**, 345–364.
- KAWAMURA, T. & KUWAHARA, K. 1984 Computation of high Reynolds number flow around a circular cylinder with surface roughness. *AIAA Paper* 84-0340.
- KOH, C. G., ZHANG, Y. & QUEK, S. T. 1999 Low-tension cable dynamics: Numerical and experimental studies. *J. Engng Mech.* **125**, 347–354.
- KUNZ, P. J. & KROO, I. 2001 Analysis and design of airfoils for use at ultra-low Reynolds numbers. In *Fixed and Flapping Wing Aerodynamics for Micro Air Vehicle Applications* (ed. T. J. Mueller), pp. 35–60. AIAA.
- LI, M. & TANG, T. 2001 A compact fourth-order finite difference scheme for unsteady viscous incompressible flows. *J. Sci. Comput.* **16**, 29–45.
- LI, Y. 1997 Wavenumber-extended high-order upwind-biased finite-difference schemes for convective scalar transport. *J. Comput. Phys.* **133**, 235–255.
- LIAO, J. C., BEAL, D. N., LAUDER, G. V. & TRIANTAFYLLOU, M. S. 2003a Fish exploiting vortices decrease muscle activity. *Science* **302**, 1566–1569.
- LIAO, J. C., BEAL, D. N., LAUDER, G. V. & TRIANTAFYLLOU, M. S. 2003b The Kármán gait: Novel body kinematics of rainbow trout swimming in a vortex street. *J. Expl Biol.* **206**, 1059–1073.
- MORETTI, P. M. 2003 Tension in fluttering flags. *Intl J. Acoust. Vib.* **8**, 227–230.

- MORETTI, P. M. 2004 Flag flutter amplitudes. In *Flow Induced Vibrations, Paris, July 6–9 2004* (ed. de Langre & Axisa), pp. 113–118. Ecole Polytechnique.
- OLSON, C. L. & OLSSON, M. G. 1991 Dynamical symmetry breaking and chaos in Duffing's equation. *Am. J. Phys.* **59**, 907–911.
- PAIDOUSSIS, M. P. 1966 Dynamics of flexible cylinders in axial flow. *J. Fluid Mech.* **26**, 717–751.
- PROCACCIA, I. 1988 Universal properties of dynamically complex systems: the organization of chaos. *Nature* **333**, 618–623.
- SARPKAYA, T. 1979 Vortex-induced oscillations. *J. Appl. Mech.* **46**, 241–258.
- SHELLEY, M., VANDENBERGHE, N. & ZHANG, J. 2005 Heavy flags undergo spontaneous oscillations in flowing water. *Phys. Rev. Lett.* **94**, 094302–1–4.
- SHEN, L., ZHANG, X., YUE, D. K. P. & TRIANTAFYLLOU, M. S. 2003 Turbulent flow over a flexible wall undergoing a streamwise travelling wave motion. *J. Fluid Mech.* **484**, 197–221.
- STRIKWERDA, J. C. 1997 High-order-accurate schemes for incompressible viscous flow. *Int'l J. Numer. Methods Fluids* **24**, 715–734.
- TECHET, A. H., HOVER, F. S. & TRIANTAFYLLOU, M. S. 1997 Separation and turbulence control in biomimetic flows. *Flow, Turb. Combust.* **24**, 715–734.
- THOMA, D. 1939 Das schlenkernde Seil (the oscillating rope). *Z. Angew. Math. Mech.* **19**, 320–321.
- THOMPSON, J. F., THAMES, F. C. & MASTIN, C. W. 1977 TOMCAT: A code for numerical generation of boundary-fitted curvilinear coordinate systems on fields containing any number of arbitrary two-dimensional bodies. *J. Comput. Phys.* **24**, 274–302.
- TRIANAFYLLOU, G. S. 1992 Physical condition for absolute instability in inviscid hydroelastic coupling. *Phys. Fluids A* **4**, 544–552.
- TRIANAFYLLOU, M. S. & HOWELL, C. T. 1994 Dynamic response of cables under negative tension: an ill-posed problem. *J. Sound Vib.* **173**, 433–447.
- WATANABE, Y., SUZUKI, S., SUGIHARA, M. & SUEOKA, Y. 2002 An experimental study of paper flutter. *J. Fluids Struct.* **16**, 529–542.
- WILLIAMSON, C. H. K. & GOVARDHAN, R. 2004 Vortex-induced vibrations. *Annu. Rev. Fluid Mech.* **36**, 413–455.
- WILLIAMSON, C. H. K. & ROSHKO, A. 1988 Vortex formation in the wake of an oscillating cylinder. *J. Fluids Struct.* **2**, 355–381.
- WOLF, A., SWIFT, J. B., SWINNEY, H. L. & VASTANO, J. A. 1985 Determining Lyapunov exponents from a time series. *Physica D* **16**, 285–317.
- ZHANG, J., CHILDRESS, S., LIBCHABER, A. & SHELLEY, M. 2000 Flexible filaments in a flowing soap film as a model for one-dimensional flags in a two-dimensional wind. *Nature* **408**, 835–839.
- ZHU, L. & PESKIN, C. S. 2002 Simulation of flapping flexible filament in a flowing soap film by the immersed boundary method. *J. Comput. Phys.* **179**, 452–468.
- ZHU, L. & PESKIN, C. S. 2003 Interaction of two flapping filaments in a flowing soap film. *Phys. Fluids* **15**, 1954–1960.
- ZHU, Q., LIU, Y., TJAVARAS, A. A., TRIANTAFYLLOU, M. S. & YUE, D. K. P. 1999 Mechanics of nonlinear short-wave generation by a moored near-surface buoy. *J. Fluid Mech.* **381**, 305–335.